1	
2	
3	Vertical Motions in Orographic Cloud Systems over the Payette River Basin.
4	Part 2: Fixed and Transient Updrafts and their Relationship to Forcing
5	
6 7 8 9	Troy J. Zaremba <sup>1</sup> , Kaylee Heimes <sup>1</sup> , Robert M. Rauber <sup>1</sup> , Bart Geerts <sup>2</sup> , Jeffrey R. French <sup>2</sup> , Coltin Grasmick <sup>2</sup> , Sarah Tessendorf <sup>3</sup> , Lulin Xue <sup>3</sup> , Katja Friedrich <sup>4</sup> , Roy M. Rasmussen <sup>3</sup> , Melvin L. Kunkel <sup>5</sup> , and Derek R. Blestrud <sup>5</sup>
10 11 12	<sup>1</sup> Department of Atmospheric Sciences, University of Illinois Urbana-Champaign, Urbana, Illinois
13	<sup>2</sup> Department of Atmospheric Sciences, University of Wyoming, Laramie, Wyoming
14 15	<sup>3</sup> Research Applications Laboratory, National Center for Atmospheric Research, Boulder, Colorado
16 17	<sup>4</sup> Department of Atmospheric and Oceanic Sciences, University of Colorado-Boulder, Boulder, Colorado
18	<sup>5</sup> Department of Resource Planning and Operations, Idaho Power Company, Boise, Idaho
19	
20	
21 22	Submitted to the Journal of Applied Meteorology and Climatology
23 24 25 26 27 28 29 30 31	Corresponding Author: Troy J. Zaremba University of Illinois Urbana-Champaign 4044 Natural History Building 1301 W. Green St Urbana, IL, 61801 815-245-0031 tzaremb2@illinois.edu

# 32 Abstract

33

34

35

36

37

38

39

40

41

42

43

44

45

46

47

48

49

50

51

Updrafts in wintertime cloud systems over mountainous regions can be described as fixed, mechanically driven by the terrain under a given ambient wind and stability profile (i.e., vertically propagating gravity waves), and transient, related to vertical wind shear and conditional instability within passing weather systems. This analysis quantifies the magnitude of fixed and transient updraft structures over the Payette River Basin sampled during the Seeded and Natural Orographic Wintertime Clouds: the Idaho Experiment (SNOWIE). Vertical motions were retrieved from Wyoming Cloud Radar measurements of radial velocity using the algorithm presented in Part 1. Transient circulations were removed and fixed orographic circulations were quantified by averaging vertical circulations along repeated cross sections over the same terrain during the campaign. Fixed orographic vertical circulations had magnitudes of 0.3-0.5 m s<sup>-1</sup>. These fixed vertical circulations comprised a background circulation in which transient circulations were embedded. Transient vertical circulations are shown to be associated with transient wave motions, cloud top generating cells, convection, and turbulence. Representative transient vertical circulations are illustrated and data from rawinsondes over the Payette River Basin are used to infer the relationship of the vertical circulations to shear and instability. Maximum updrafts are shown to exceed 5 m s<sup>-1</sup> within Kelvin-Helmholtz waves, 4 m s<sup>-1</sup> associated with transient gravity waves, 3 m s<sup>-1</sup> in generating cells, 6 m s<sup>-1</sup> in elevated convection, 4 m s<sup>-1</sup> in surface-based deep convection, 5 m s<sup>-1</sup> in boundary layer turbulence, and 9 m s<sup>-1</sup> in shear-induced turbulence.

#### 1. Introduction

Quasi-stationary orographically-induced gravity waves result from winds that blow across a mountain range causing forced ascent on the windward side and forced descent on the leeward side. The behavior of these vertically propagating waves in response to ambient stability and wind profiles have been studied extensively, mainly through numerical simulations with idealized terrain and idealized soundings (see review by Smith 2018). Cross-mountain distributions of forced ascent/descent are dependent on terrain geometry such as the height, width, and length of a given mountain range (e.g., Sinclair et al. 1997, Chater and Sturman 1998, see Chapter 5 in Lin 2009 for a review). In general, the quasi-stationary updraft and downdraft intensity varies proportionally with the strength of the mean low-level winds (e.g., Held and Ting 1990; Colle 2004).

Most mountain ranges on Earth exhibit complex terrain profiles, with 2D terrain width, heights, and length "felt" by the wind that depend on the prevailing wind direction. Wave behavior is different for different individual ridges, and the mesoscale flow over these ridges is impacted by the entire mountain range. To a first order, in an unsheared environment, a mountain ridge will produce a vertically-propagating gravity wave if the advective time scale exceeds the time scale of buoyancy oscillations. That is, the mountain width must exceed  $U\pi/N$ , where U is the ridge-normal wind speed, and N the Brunt-Väisälä frequency (see Chapter 5 in Lin 2009; Hunt et al. 1998; Vasper et al. 2002, Lyza and Knupp 2018). Under strong winds and weak (moist) stratification, as is common when frontal disturbances cross a mountain range, only the larger ridges produce a wave response. Smaller ridges produce "evanescent" waves, i.e. a shallow dipole of rising/sinking flow on the upstream/lee side of the ridge. The interaction between serial vertically-propagating gravity waves, and between the hydrometeors they produce in moist flow (Reinking et al. 2000; Bruintjes et al. 1994), is poorly understood.

Although orographically-forced updrafts are commonly present, the nature of the updrafts can be modified by a variety of transient processes, the main one being convection. The focus here is on cold-season storms. While these orographic clouds are primarily stratiform, they often contain shallow to deep embedded convection, generally the result of the release of potential instability by orographic lifting (Shafer et al. 2006; Ikeda et al. 2007; Geerts et al. 2015; Kirshbaum et al. 2018). Other, typically smaller-scale transient updrafts can be associated with cloud-top generating cells (e.g., Kumjian et al. 2014, Keeler et al. 2016a,b, 2017), with shear-induced Kelvin-

Helmholtz billows and associated turbulence (Houze and Medina 2005; Medina and Houze 2015, Grasmick and Geerts 2020, Grasmick et al. 2021), or with boundary layer turbulence (Geerts et al. 2011; Chu et al. 2018). Quantifying the properties and magnitudes of fixed and transient updraft structures within orographic clouds is a crucial step towards understanding where and when supercooled water may be present and where wintertime orographic cloud seeding opportunities may exist.

The Seeded and Natural Orographic Wintertime Clouds: the Idaho Experiment (SNOWIE; Tessendorf et al. 2019) provided an opportunity to address questions related to orographic updraft structures. SNOWIE was carried out over the Payette River Basin of western Idaho from 7 January to 16 March 2017. During that time 23 research flights took place during intensive operation periods (IOPs). The SNOWIE project is particularly interested in quasi-stationary updrafts, and their supercooled liquid water, as those updrafts may be targetable for glaciogenic seeding to enhance precipitation. Previous work has addressed the impact of airborne seeding with silver iodide aerosol (French et al. 2018; Friedrich et al. 2020, 2021).

The purpose of this paper is to analyze the magnitude, vertical distribution, and forcing of vertical air motions in orographic cloud systems over the Payette River Basin during SNOWIE. Data used in this analysis is presented in Sec. 2. An overview of the orography associated with the Payette River Basin is given in Sec. 3. A composite analysis quantifying the magnitude and distribution of fixed orographic waves will be presented in Sec. 4 along with a comparison of composite updraft structure from a 900 m resolution simulation from the Weather Research and Forecasting Model (WRF). In Sec. 5, transient updraft structures are examined and related to thermodynamic and wind profiles measured by special project rawinsondes. Individual case studies of transient updrafts associated with wave motions, cloud top processes, convection, and turbulence are presented. Key findings are summarized in Sec. 6.

#### 2. Data and Methodology

a) Wyoming Cloud Radar and Updraft Retrieval Overview

The University of Wyoming Cloud Radar (WCR; e.g. Wang et al. 2012) is a 95 GHz, 3 mm wavelength, pulsed Doppler cloud radar that was flown on the University of Wyoming King Air (UWKA) during SNOWIE. During SNOWIE the UWKA flew back and forth flight legs along one of three flight tracks (Fig. 1a,b). One flight leg was typically completed in 10-20 minutes, with 4-hour flights typically completing 10-14 flight legs. Data used herein are from the WCR fixed

antennas nominally pointed at zenith and nadir during straight, level flight. In this configuration, the WCR measured the equivalent reflectivity factor  $(Z_e)$  and radial velocity  $(V_r)$ . Data was sampled at 30 m range resolution along the radar beams and 4.5 to 7.5 m along the flight track depending on the ground-relative aircraft speed. The WCR reflectivity is calibrated by measuring the return from a trihedral corner reflector with a known scattering cross-section. Error associated with this calibration is estimated to be less than 2.5 dB at and away from the radar flight level (Wendisch and Brenquier 2013, Ch. 9.5.5, pp. 509-517; Grasmick et al. 2022). The minimum detectable signal was ~-40 dBZ<sub>e</sub> at 1 km distance away from the radar and ~-26 dBZ<sub>e</sub> at a distance of 5 km. Measurements of  $Z_e$  and  $V_r$  were available between the ground and cloud top except in a 250 m blind zone centered at flight level. Zaremba et al. (2022, Part 1) presented an algorithm to retrieve vertical velocity (w) and flight-leg-averaged mean reflectivity-weighted particle terminal velocity  $(\overline{V_t})$  as a function of altitude for each flight leg during SNOWIE. The retrieval technique involves using rawinsonde-measured winds to retrieve W, the vertical hydrometeor velocity at a given range gate, by removing contributions of the aircraft motion and the horizontal wind to V<sub>r</sub> due to time-dependent variations in the beam-pointing vector resulting from small fluctuations in pitch, roll, and yaw of the aircraft due to flight-level turbulence or pilot adjustments while flying along straight flight legs (Zaremba et al. 2022, Part 1). The mean W,  $(\overline{W})$ , at a given height was assumed to be the mean reflectivity weighted terminal velocity,  $\overline{V}_t$ , at that height allowing for the retrieval of w. The accuracy of the retrieval of w and  $\overline{V}_t$  was shown to be dependent on satisfying assumptions that the legs occur over a short enough time and distance that the along- and acrosstrack winds at a given altitude above/below the aircraft do not vary horizontally or change with time, the magnitudes of the updrafts and downdrafts across the flight track at any given altitude sum to 0 m s<sup>-1</sup>, and that  $\overline{V}_t$  did not vary substantially along a given flight leg at a given altitude. A method to estimate the uncertainty in the retrieval of w as a function of altitude was presented based on evaluation of these assumptions. The reader is referred to Part 1 for details of their uncertainty analysis. Uncertainty estimates using the Zaremba et al. (2022) methodology are included with each case study herein. Updrafts and downdrafts mentioned herein refer to vertical air motion, w, not hydrometeor vertical motion. Contoured Frequency by Altitude Diagrams (CFADs) are used to quantify the magnitudes of orographic updraft and downdraft structures observed during SNOWIE. CFADs were binned in increments of 0.1 m s<sup>-1</sup> and by altitude in 100 m increments, except in the lowest 100 m to avoid terrain contamination.

114

115

116

117

118

119

120

121

122

123

124

125

126

127

128

129

130

131

132

133

134

135

136

137

138

139

140

141

142

143

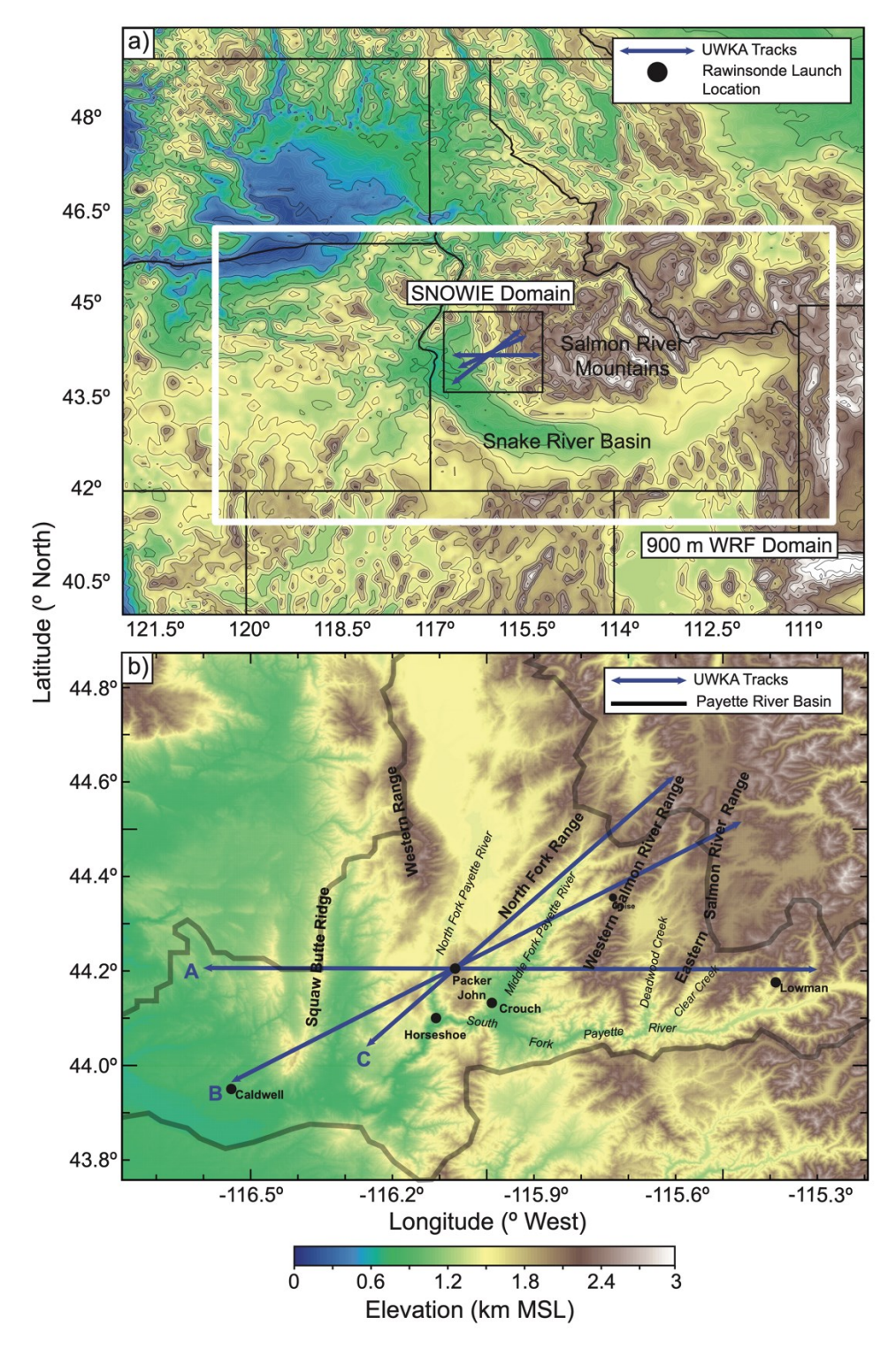


Fig. 1: a: SNOWIE domain outlined in black. Domain of 900 m WRF simulations outlined in white. Elevation (0.125° x 0.125° grid) in meters above MSL is contoured. Plotted in blue are the three flight tracks flown during SNOWIE. Rawinsonde launch locations are noted by black dots. b: Same as (a) except 900 m SNOWIE domain terrain elevation. The Payette River Basin is outlined in black. Ranges and valleys are labeled.

#### b) Rawinsondes

The Idaho Power Company (IPC) launched Lockheed Martin LMS6 rawinsondes from sites in Crouch and Lowman, ID (Fig. 1a,b). The University of Illinois Urbana-Champaign (UIUC) launched iMet-1 rawinsondes from Boise, ID and Caldwell, ID. These rawinsondes were used herein to characterize the environment when various mesoscale updraft structures were observed. The manufacturer-stated accuracy of IPC rawinsondes was  $\pm 0.2$ °C for temperature,  $\pm 0.2$  m s<sup>-1</sup> for wind,  $\pm 5$ % for relative humidity, and  $\pm 0.5$  hPa for pressure. The manufacturer-stated accuracy of UIUC rawinsondes was  $\pm 0.2$ °C for temperature,  $\pm 1$  m s<sup>-1</sup> for wind speed,  $\pm 5$ % for relative humidity, and  $\pm 0.5$  hPa for pressure. Rawinsonde data collected during SNOWIE typically had an average resolution of 4 m and drifted an average of 12.4 km away from their launch location between the surface and cloud top.

Kirshbaum and Durran (2004) have shown that determining static stability in orographic precipitation requires evaluation of the moist Brunt-Väisälä frequency ( $N_m$ ) originally derived by Lalas and Einaudi (1974) as:

$$N_m^2 = \frac{g}{T} \left( \frac{dT}{dz} + \Gamma_m \right) \left( 1 + \frac{Lq_s}{R_d T} \right) - \frac{g}{1 + q_w} \frac{dq_w}{dz}$$

Instability exists where  $N_m$  is imaginary. In the equation above, g is gravity, T is temperature, L is the latent heat of condensation,  $\Gamma_m$  is the moist adiabatic lapse rate,  $R_d$  is the dry air gas constant,  $q_s$  is the saturation mixing ratio, and  $q_w$  is the total water mixing ratio. Kirshbaum and Durran (2004) note that a negative vertical gradient in equivalent potential temperature ( $\theta_e$ ) is generally insufficient to evaluate potential instability. Using  $N_m$  is particularly important in cases of extreme orographic rainfall such as convection associated with flooding events, like the Big Thompson flood (Caraceña et al. 1979), and the generation of mesoscale convective systems (e.g. Chu and Lin 2000). Herein, our analysis of potential instability during convective events is limited to rawinsonde data. Wintertime orographic clouds over the Payette River Basin are primarily ice clouds containing only small, localized amounts of cloud water (typically  $q_l = 10^{-4}$ ). The mass of ice particles ranges from  $\sim 10^{-10}$  kg for unrimed plate like particles (Itoo et al. 1954) to  $\sim 10^{-7}$  kg for heavily rimed ice particles (Locatelli and Hobbs 1974). Typical concentrations of ice in wintertime orographic clouds are  $\sim 20$  L<sup>-1</sup> (Rauber 1987). The ice mixing ratio ( $q_i$ ) in conditions of no riming at a pressure of 700 mb is of order of  $10^{-6}$ , while in heavily rimed conditions the ice mixing ratio at 700 mb can approach  $10^{-3}$ . Unfortunately, no information, even from aircraft data, is available

to determine the vertical gradient of the liquid water mixing ratio  $(q_l)$  and  $q_i$ , and thus  $q_w$ . Herein, the presence of potential instability is evaluated using vertical gradients in  $\theta_e$  measured by nearby rawinsondes, while acknowledging that the mass of ice and supercooled water particles will have a negative influence on buoyancy.

Wind speed,  $\theta_e$ , Bulk Richardson Number ( $R_i$ ), Scorer parameter ( $\ell^2$ ), and vertical wind shear (|S|) were calculated from the rawinsonde data and used together with w to interpret the thermodynamic and shear environment in which updrafts and downdrafts occurred. In each case, the nearest rawinsonde in time was chosen for analysis. We use  $\theta_e$  with respect to water calculated using Bolton et al. (1980), rather than  $\theta_e$  with respect to ice, because it provides a more stringent criterion for the detection of regions of potential instability (e.g. Kumjian et al. 2014). Rawinsonde data were averaged using a centered rolling mean over 20 data points ( $\sim$ 100 m) and resampled using linear interpolation every 100 m, when calculating  $R_i$ :

193 
$$R_{i} = \frac{g}{\overline{\theta_{v}}} \frac{\frac{\Delta \theta_{v}}{\Delta z}}{\left(\frac{\Delta u}{\Delta z}\right)^{2} + \left(\frac{\Delta v}{\Delta z}\right)^{2}}$$

where u and v are the parallel and normal wind components, z is the rawinsonde height, and  $\theta_v$  is the mean virtual potential temperature where:

$$\overline{\theta_v} = \frac{\theta_{v,top} + \theta_{v,bottom}}{2}$$

197 and:

$$\theta_v = \theta(1 + 0.61r)$$

where r is the mixing ratio.

 $\ell^2$  (m<sup>-2</sup>) is defined as:

$$\ell^2 = \frac{N_m^2}{U^2} - \frac{\frac{\partial^2 U}{\partial z^2}}{U}$$

where U = U(z) is the horizontal wind at a given height, was used to diagnose layers where trapping of low-level gravity waves could have occurred. To calculate  $\ell^2$  a second rolling mean of the 100 m resampled sounding dataset was calculated centered over 1 km. The condition  $\ell^2 < 0$  is favorable for gravity wave trapping (Crook 1988). For the case of gravity waves,  $\ell^2$  was calculated using the Moist Brunt-Väisälä frequency noted in Kirshbaum and Durran (2004) except  $q_w$  was approximated by  $q_s$ .

Vertical wind shear was calculated by using a centered rolling mean over 20 rawinsonde data points (~100 m):

$$|S| = \sqrt{\left(\frac{\Delta u}{\Delta z}\right)^2 + \left(\frac{\Delta v}{\Delta z}\right)^2}$$

## c) WRF Model Configuration

During the winter season of 2016-2017, WRF version 3.9.1.1 was run in a continuous simulation starting on 1 October and ending on 30 April, which included the entire SNOWIE campaign. Nested simulations were run with 2700 m (outer) and 900 m (inner) horizontal grid resolutions. The 900 m domain had 81 terrain following vertical levels between the surface and 20 hPa distributed with 23 levels below 1 km above ground level (AGL) and 43 levels below 3 km AGL. WRF model runs were initialized using ERA-Interim data (Dee et al. 2011). Table 1 summarizes the model configurations used. The southeastern part of the 900 m domain is outlined in Fig. 1a. Hourly WRF model output of vertical motion fields along the flight tracks at the time of the flights were used to compare modeled and retrieved fixed orographically-forced updrafts and downdrafts over the Payette River Basin.

	2700 m Domain	900 m Domain
Model Version	WRF version 3.9.1.1	WRF version 3.9.1.1
Horizontal Grids	540 x 360	450 x 300
Time Step	10 s	3 s
Driving Data	ERA-Interim	One-way nest from 2.7 km
		domain WRF outputs
Vertical Coordinate		81 terrain-following eta levels
Land Surface Model		Noah MP
Radiation		RRTMG LW & SW
Planetary Boundary	MYNN	MYNN
Layer Scheme		
Microphysics	Thompson-Eidhammer (TE	TE and TE with AgI seeding
	Thompson and Eidhamer	parameterization (Xue et al.
	2014) with Cooper (1986) ice	2013a,b) with Cooper (1986)
	nucleation option	ice nucleation option

Table 1: NCAR WRF model configuration.

## 3. Orography of the Payette River Basin

The Salmon River Mountains, an extensive block-shaped massif which is part of the Central Rocky Mountains, cover the central part of the state of Idaho (Fig. 1a). The Salmon River

and its tributaries drain the northern side of the mountains while the Payette River and its tributaries drain the south and west side. The entire massif is west of the Continental Divide and water falling on the Salmon River mountains eventually drains into the Snake and Columbia River Basin.

The mountain massif on its southwest side encompasses the Payette River Basin and consists of a series of ridges and valleys which run primarily north-south (Fig. 1b). The ridges reach elevations of ~2.5 to 2.8 km while the upper valleys have elevations of ~1.4 km, descending to ~0.9 km along the South Fork of the Payette River at Crouch, Idaho where rawinsondes were launched during SNOWIE. The Snake River Basin is a nearly-enclosed depression (Fig. 1a), with water exiting through the deep, narrow Hells Canyon in the northeast. Under stratified conditions (as commonly occurs in winter when a frontal disturbance advects warm moist air well above the Snake River Basin), near-surface air usually is advected from the southeast near Boise, and from the south in the valleys of the Payette River Basin (Tessendorf et al. 2019).

The UWKA during SNOWIE flew back and forth (typically west-east, or southwest-northeast) legs along one of three tracks over the Payette River Basin parallel to the mid-level (~700 hPa) flow (Fig. 1b). On the west-east flight track (A on Fig. 1b) the UWKA crossed the Squaw Butte ridge, the southern end of the Western Range, the North Fork Range, and the Western and Eastern Salmon River ranges, as well as the Payette River tributaries between these ranges. On track B, the UWKA flew over the same ranges but at a ~40° angle to the ridge lines. On track C, the UWKA crossed the Western Range and flew along the eastern side of the North Fork Range, crossing the pass at the northern limit of the Middle Fork of the Payette River (Fig. 1b). Vertical motions observed during SNOWIE reported in this paper were associated with forcing fixed to this topography and transient circulations within passing weather systems.

## 4. Vertical Motions associated with fixed orographic forcing

Vertical motions forced by orography are approximately fixed relative to the topographic relief, their magnitudes determined by the wind near and over the terrain, the terrain steepness and stability. During SNOWIE, the UWKA flew consecutive back and forth flight legs along one of three flight tracks parallel to mean midlevel flow, completing 238 total flight legs. This allowed for composites of vertical motion (w) from many flight legs to be constructed along fixed tracks over the terrain. Because transient circulations vary in time and space, averaging the vertical motion fields over a large number of flight legs has the effect of removing transient updrafts while retaining fixed vertical circulations. In this section, we present composite radar-retrieved  $\overline{w}$  for a

large number of flight legs using all available data from SNOWIE to determine the average magnitude of ascent/descent forced by fixed orographic circulations. The composite retrieved  $\overline{w}$  fields associated with fixed orographic waves are then compared to similar composite  $\overline{w}$  fields retrieved from the 900 m resolution WRF simulation for the same times as the aircraft sampling.

For each flight leg, w was retrieved on a common 30 m vertical grid and then averaged at a given height every  $0.005^{\circ}$  longitude.  $\overline{w}$  was then calculated for each flight track by averaging w at a given height and longitude for all regridded flight legs. Each grid point had to have at least 10 flight legs averaged at a given height/longitude to be included in the composite. Heights below 2.5 km (all heights above sea level) were not included in the composites because they were contaminated by terrain and/or melting in the valleys. Only two flight tracks (Fig. 1b tracks A and B) had a sufficient number of flight legs to create composites. A composite for the third track (Fig. 1b track C) was not calculated due to an insufficient number of legs.

Fig. 2a shows the number of flight legs at each grid point used to construct the composite for flight track A (Fig. 1b). Eight research flights (82 flight legs) were used in the composite. Different grid points had less than 82 samples in the composite for two reasons. First, the WCR has nadir and zenith pointing beams but is unable to retrieve radar data in a 250 m vertical zone centered at the flight level. The aircraft typically flew at lower altitudes < 6 km in order to sample potential seeding signatures. The blind zone routinely shows up as thin strips of lower counts in the composite of the total number of flight legs. Second, larger regions of missing data at higher elevations were the result of split cloud layers and variations in the cloud depth. In all composited flight legs for track A, the mean midlevel flow over the terrain was westerly, near-parallel to the flight legs.

Large scale orographic waves are evident over the terrain in the composite  $\overline{w}$  analysis (Fig. 2b). Orographically forced updrafts and downdrafts are present on the windward and leeward sides of the Western Range, North Fork Range, Western Salmon River Range, and Eastern Salmon River Range, respectively, each on the order of  $\pm 0.3$ -0.5 m s<sup>-1</sup> (Fig. 2c). The orographic wave crests slope upwind with height, consistent with wave theory (Smith et al. 2018). The strongest updrafts (0.4-0.5 m s<sup>-1</sup>) were located over the Western Salmon River Range (which has the steepest terrain) between -115.8° and -115.6° longitude. Updraft magnitudes decreased with height with maximum/minimum  $\overline{w}$  found near the terrain. A standing wave was also present west and over the narrow North Fork Valley between -116.3° and -116.1° longitude (Fig. 2b). Fig. 2d shows  $\overline{w}$  from

the WRF simulation averaged over all hourly output during the SNOWIE research flights composited in Fig. 2b. The modeled  $\overline{w}$  closely mirrors the radar-retrieved  $\overline{w}$  in Fig. 2b in terms of orographic wave structure, location, and magnitude ( $\pm 0.3$ -0.5 m s<sup>-1</sup>, Figs. 2d,e) including the standing wave west and over the North Fork Valley, lending confidence to the radar-retrieved  $\overline{w}$  composite.

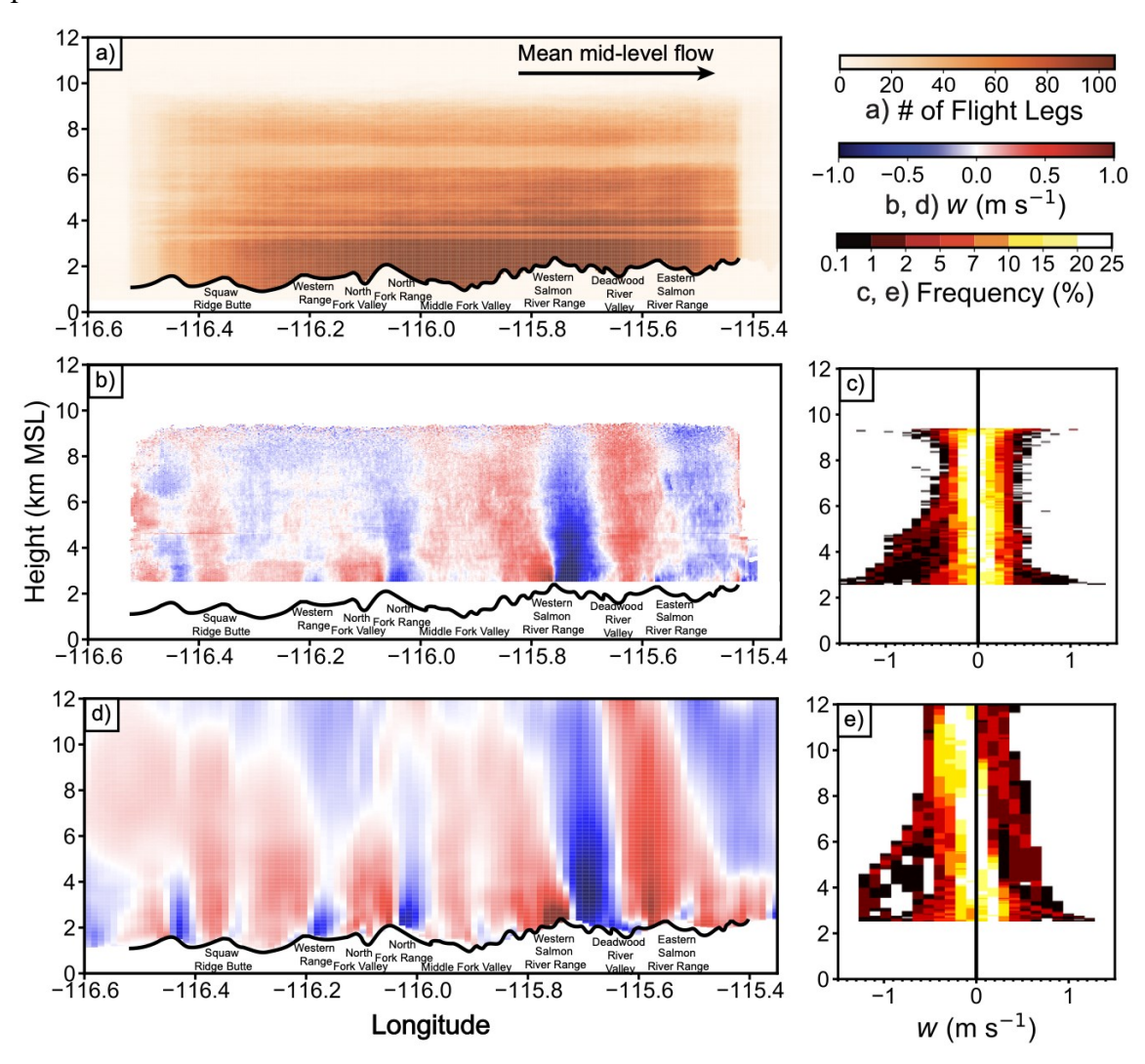


Fig. 2: West-east cross section of  $\overline{w}$  along flight track A (in Fig. 1b) during SNOWIE. a: is the number of flight legs with cloud present at a given height binned every 30 m and 0.005° longitude. b:  $\overline{w}$  in a given  $0.005^{\circ}$  (~400 m) longitude range at a given height. c: CFAD of  $\overline{w}$  binned every 100 m and 0.1 m s<sup>-1</sup>. d: 900 m WRF  $\overline{w}$  during the same research flights. e: CFAD of 900 m WRF  $\overline{w}$  binned every 100 m and 0.1 m s<sup>-1</sup>. Includes flight legs from 8 different research flights (IOP01, IOP03, IOP09, IOP11, IOP12, IOP21, IOP22, and IOP23). Significant terrain features of the Payette River Basin are noted.

Note that a wide range such as the Western Salmon River Range supports a gravity wave that propagates vertically to at least 12 km, whereas a narrow ridgeline such as Squaw Butte triggers a far shallower wave (Fig. 2b and c). Linear theory, with wind speed (U) and the Brunt-Väisälä frequency (N), both constant with height, predicts vertically propagating evanescent waves over a sinusoidal mountain with width  $\lambda < \frac{2\pi U}{N}$  and vertically propagating waves when  $\lambda > \frac{2\pi U}{N}$  (Durran 1990). The wavelength ( $\lambda$ ) for Squaw Butte is about 2.6 km while the  $\lambda$  for the Western Salmon Range was ~20 km. Although the wind speed and the Brunt-Väisälä frequency varied from hour to hour and were not constant with height, the wavelength of Squaw Butte is only 10% of the Western Salmon River Range, so linear theory suggests that the Western Salmon Range is more likely to produce vertically-propagating quasi-stationary vertical motions.

To compare the radar observations and model in the composite, it is assumed that the flow is 2D and that these cross sections provide a realistic (e.g., west to east) depiction of flow over and above the terrain. The flow, however, often veered with height at lower levels due to southerly flow in the valleys as indicated by the CFAD of wind speed and direction in Fig. 3a,b of the 38 rawinsondes launched during the composited flight legs. Winds near the surface were typically weak and out of the south (between 0-5 m s<sup>-1</sup> with 90% of surface winds < 15 m s<sup>-1</sup>) but increased significantly with height, ranging from 35 to 65 m s<sup>-1</sup> at 8 km, (10<sup>th</sup> to 90<sup>th</sup> percentile), rapidly veering to westerly above the valley floors and through most of the depth of the cloud. The abundance of transient fine-scale updrafts present over the terrain are heavily influenced by vertical drafts associated with stationary terrain driven waves seen in both the radar *w* composite and 900 m model output composite.

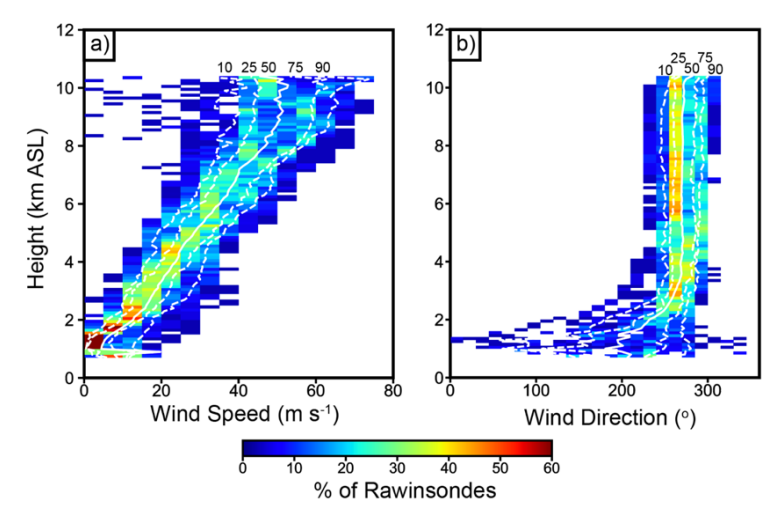


Fig. 3: CFAD of 38 rawinsondes during the 8 different research flights (IOP01, IOP03, IOP09, IOP11, IOP12, IOP21, IOP22, and IOP23) composited in Fig. 2. Rawinsonde wind speed and wind direction were resampled every 100 meters (interpolated to a given altitude). A given altitude had to have at least 10 rawinsonde data points in order to be included in the CFADs. a: wind speed every 100 meters from all 38 rawinsondes binned every 5 m s<sup>-1</sup>. b: wind direction every 100 meters from all 38 rawinsondes binned every 10°.

Fig. 4a shows the number of flight legs at each grid point used to construct the composite for flight track B (Fig. 1b). Eleven research flights (126 flight legs) were used in the composite. Midlevel flow for these flights was southwesterly, again near-parallel to the flight track. Updrafts and downdrafts associated with fixed orographic waves were again on the order of  $\pm 0.3$ -0.5 m s<sup>-1</sup> (Figs. 4b,c) with updrafts on the windward side and downdrafts on the leeward side of the terrain. The strongest updrafts and downdrafts were associated with the steepest terrain on either side of the Western Salmon Range. Again, the modeled  $\overline{w}$  (Fig. 4d,e) closely mirrored radar-retrieved  $\overline{w}$  in Figs. 4b,c in terms of orographic wave structure, location, and magnitude. Fig. 5a,b shows wind speed and direction CFADs of the 58 rawinsondes launched over the Payette River Basin during the eleven composited research flights. Again, flow increased from an average of ~0-5 m s<sup>-1</sup> at the surface to an average of ~40 m s<sup>-1</sup> at 8 km. Low-level valley winds were again more southerly and veered with height whereas upper-level flow out of the southwest was parallel to the 2D fight track and terrain cross section.

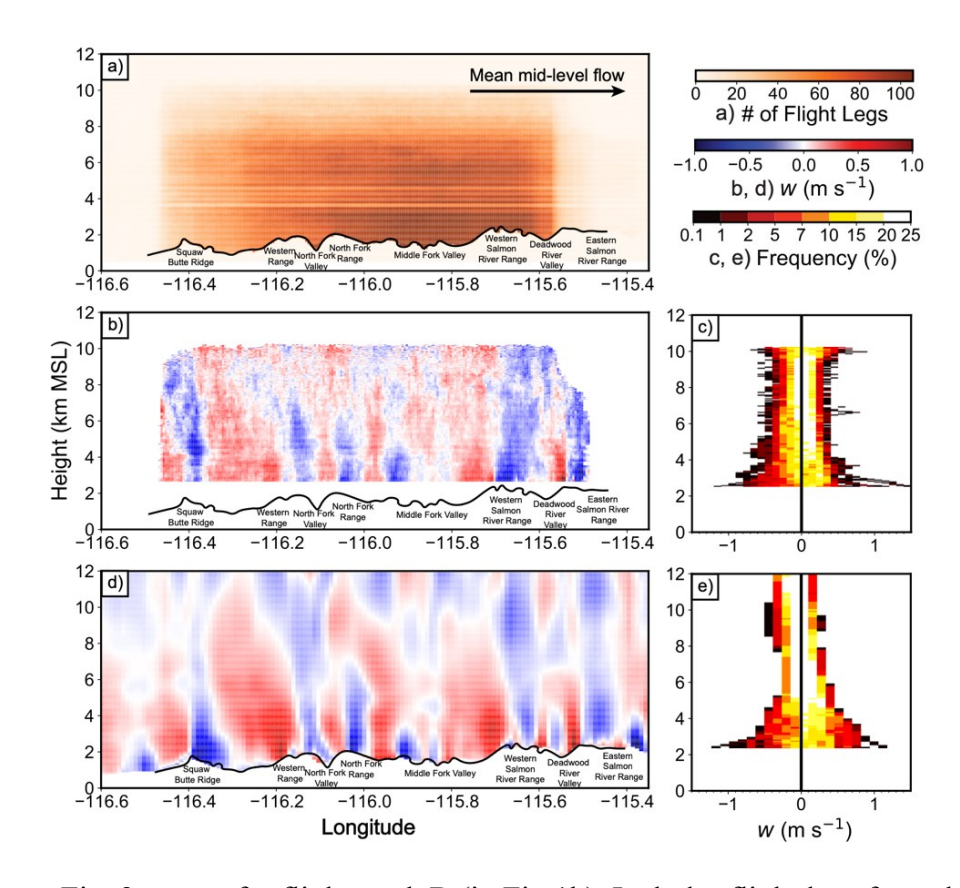


Fig. 4: Same as Fig. 2 except for flight track B (in Fig 1b). Includes flight legs from the 11 different research flights (IOP02, IOP04, IOP08, IOP10, IOP13, IOP15, IOP16, IOP17, IOP19, IOP20, and IOP24).

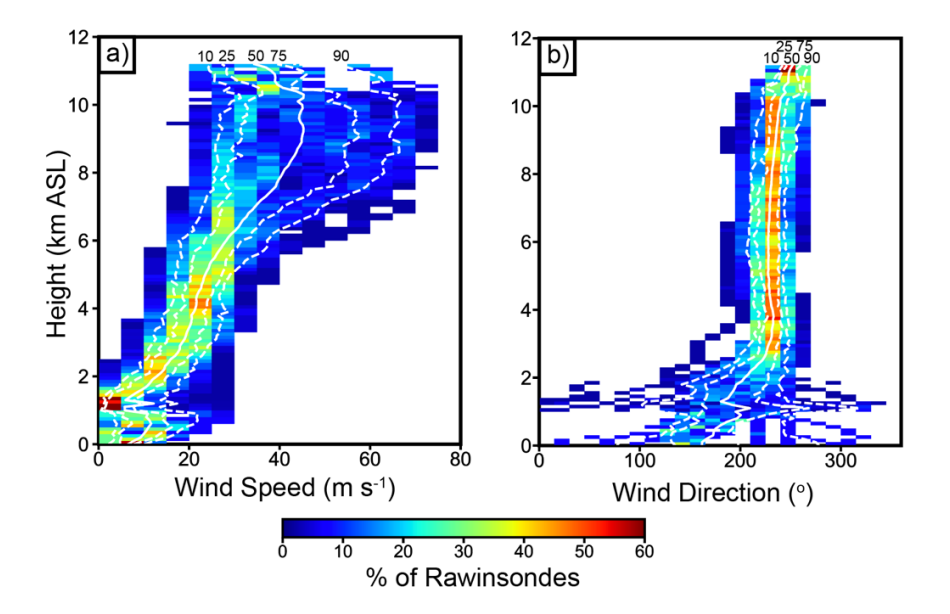


Fig. 5: Same as Fig. 3 except these CFADs represent the 58 rawinsondes launched during the 11 research flights (IOP02, IOP04, IOP08, IOP10, IOP13, IOP15, IOP16, IOP17, IOP19, IOP20, and IOP24) composited in Fig. 4.

#### 5. Vertical motions associated with transient features

Transient updraft features are associated with mesoscale circulations in weather systems passing over the mountains. In general, these can be expected to superimpose on, and interfere with, the fixed circulations discussed in Sec. 4. Transient updrafts observed were associated with wave motions, cloud top generating cells, convection, and turbulence. In this section, these transient updraft structures are related to the thermodynamic environment and shear profiles measured with nearby rawinsondes.

365 a) Wave Structures

366 i) Kelvin-Helmholtz (KH) waves

Grasmick and Geerts (2020) and Grasmick et al. (2021) analyzed KH waves during SNOWIE using dual-doppler wind retrievals from the WCR. They found that KH waves were frequently locked to the terrain and occurred at different heights, including the free troposphere, boundary layer tops, and near the surface. They also observed KH waves upwind and in the wake of steep terrain. These environments locally enhance shear, creating conditions conducive to KH waves. Vertical-plane dual-doppler analysis performed by Grasmick and Geerts (2020) revealed braided structures within KH waves that result from deforming shear layers. Because Grasmick and Geerts (2020) and Grasmick et al. (2021) provided detailed analysis of KH waves observed during SNOWIE, we limit the discussion here to an example at cloud top during IOP2 (9 January, 0200 UTC - 0900 UTC) from the tenth leg between 0718-0725 UTC.

Fig. 6a,b shows  $Z_e$  and w, respectively, along the flight leg illustrating KH waves at cloud top (~7.6 km). The region of KH waves is expanded in Fig. 6c for clarity. Data from the rawinsonde launched at 0700 UTC by UIUC is overlaid (Fig. 6c). KH waves were located west of the North Fork Range and were associated with a region of enhanced shear with wind speeds increasing from 25 m s<sup>-1</sup>at the base of the KH wave layer (5.3 km) to 55 m s<sup>-1</sup> at the top of the layer (7.6 km). |S| was 18-20 m s<sup>-1</sup> km<sup>-1</sup> between 5.3 and 7.6 km. Within the KH wave layer,  $\theta_e$  increased with height from 316 to 321 K, indicating that the layer was stable. The KH waves in this case were induced by the strong shear and broke to produce turbulence. Within the KH waves, w ranged from -5 m s<sup>-1</sup> to +5 m s<sup>-1</sup> (Fig. 6d). Beneath the waves, flow was slower than within the wave layer, and the updrafts and downdrafts were weaker, with little evidence connecting the waves to the topography (Fig. 6b,c).

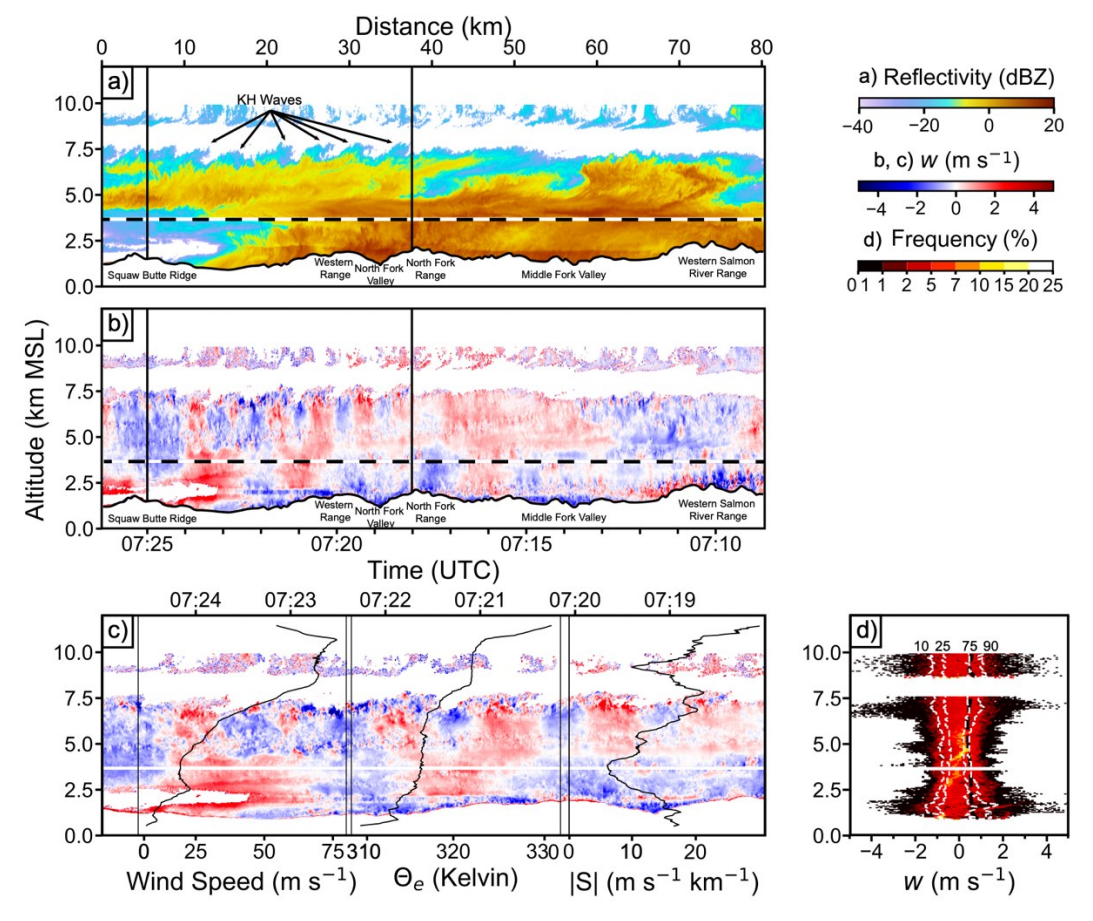


Fig. 6: WCR cross section from 9 January 2017 0709-0726 UTC along track B. a:  $Z_e$ ; b: w; c: expansion of b between 0718-0725 UTC overlaid with wind speed (this region is noted on a and b by solid black vertical lines),  $\theta_e$ , and |S| from a radiosonde launched by UIUC at 0700 UTC. d: CFAD of w in panel c binned every 100 m in altitude every 0.1 m s<sup>-1</sup>. The black dashed line on d represents w retrieval uncertainty calculated using methodology presented in Part 1. The white dashed lines represent the  $10^{th}$ ,  $25^{th}$ ,  $75^{th}$ , and  $90^{th}$  percentiles of w at a given height. Significant terrain features of the Payette River Basin are noted on a and b.

#### ii) Gravity Waves

Gravity waves not fixed to the underlying topography were occasionally observed during SNOWIE. The most extreme example occurred during IOP20 (5 March, 1200 - 1630 UTC) when gravity waves within a stably-stratified mid-tropospheric layer appeared ahead of a cold front advancing into the study area. At the altitude of the gravity wave layer, the cold front was moving eastward across the Western Idaho border at 11 m s<sup>-1</sup>, just upstream of the UWKA flight track (Fig. 7). A strong jet (up to 45 m s<sup>-1</sup> at 500 hPa) was present just ahead of the cold front.

The gravity waves appeared as a wave packet ahead of the front traversing the sample area over the course of 1 hour (Fig. 8c-g). The wind at the center of the gravity wave layer (~5 km) was

~25 m s<sup>-1</sup> out of the southwest. The wind speed together with the dimensions of the wave packet in the radar cross sections indicate that the wave packet was confined within the distance of 90 km. The wavelength within the wave packet was uniform, and unrelated to the underlying terrain. With time, the wavelength observed by the UWKA decreased from 8 to 5 km during the passage of the wave packet. Maximum updrafts and downdrafts within the gravity wave layer, between 4 and 6 km, were on the order of 6 m s<sup>-1</sup> (Fig. 8). The wave also appeared to induce vertical motions above the gravity wave layer although these vertical motions (ranging up to 3-4 m s<sup>-1</sup>) appeared more chaotic and turbulent in nature.

Fig. 9 shows a cross section of the gravity waves between 133250-134650 UTC overlaid with sounding data from a rawinsonde launched at 1300 UTC at Crouch, ID.  $\ell^2$  was negative between 4.6 and 5.8 km implying that layer was favorable for gravity wave ducting. The gravity waves occurred in a stably-stratified layer with weak wind shear (Fig. 9b). |S| was ~10 m s<sup>-1</sup> km<sup>-1</sup> in the gravity wave layer. Wind speed was near constant within the gravity wave layer, likely a result of the waves redistributing momentum within the layer. Wave motion was also evident in the reflectivity profile (Fig. 9a).

GOES-15 visible satellite imagery shows transient wave packets, not tied to the terrain, were widespread across Southern Idaho at this time (Fig. 10). The origin of the gravity wave packet is uncertain but may be tied to the advancing front based on previous studies. Ralph et al. (1999) showed examples of gravity waves propagating ahead of a cold front that resembled trapped lee waves. These prefrontal gravity waves occurred when the wave forcing decayed along the eastern portion of the front and the trapped waves propagated away from the front. In this current study, the gravity waves propagate through a region of stability ahead of the front. Li et al. (2017) showed that trapped lee waves only form if the warm sector ahead of a wintertime cold front is stably stratified. The evolution of upstream flow in their cases influenced wave structure, amplitude, and wavelength. In their study, as the cold front approached increasingly stably-stratified strong crossbarrier flow, wavelengths observed were longer and trapped lee waves extended farther downstream. After the upstream airflow weakened, the wavelength shortened, and the lee waves dissipated. These studies provide some support for the hypothesis that the gravity wave packet was influenced by the advancing front.

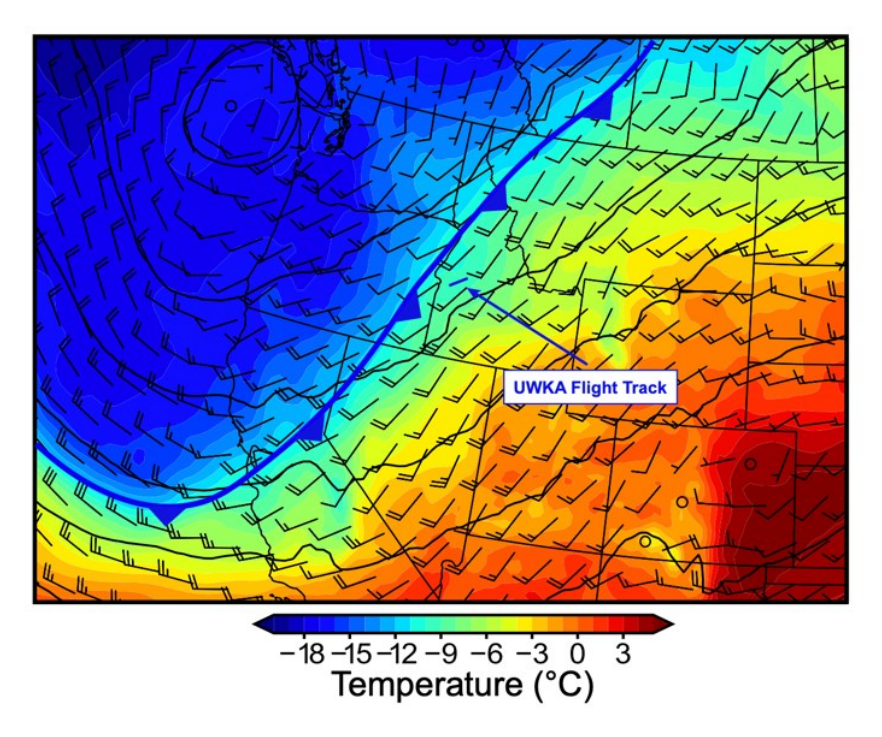


Fig. 7: 700 hPa temperature shaded, 700 hPa heights contoured, and 700 hPa wind barbs (where a half-staff is 5 m s $^{-1}$ , full staff is 10 m s $^{-1}$ , and flag is 50 m s $^{-1}$ ) valid at 1200 UTC on 5 March 2017. The cold front is labeled using standard symbology and flight track B flown during IOP20 is noted.

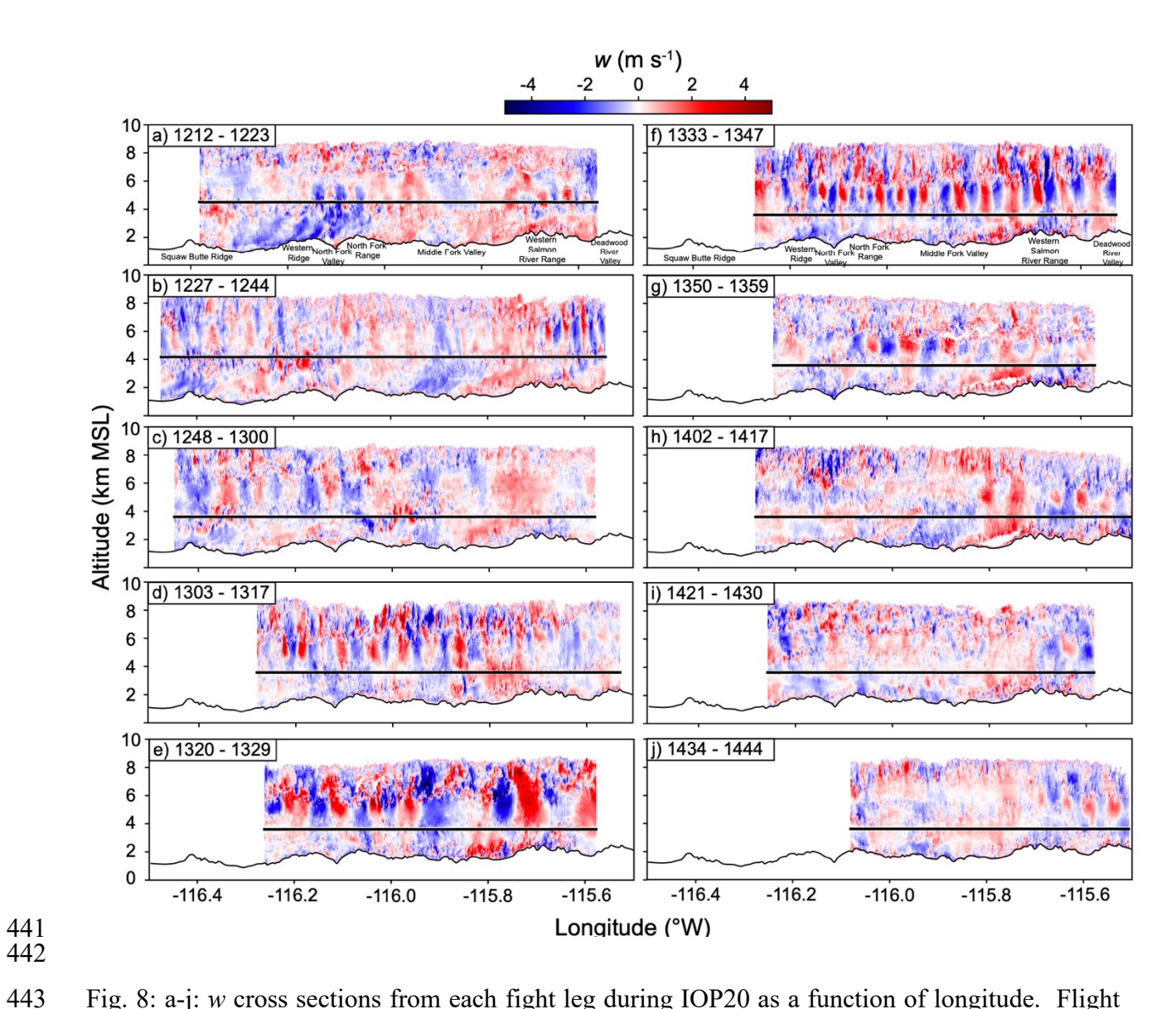


Fig. 8: a-j: w cross sections from each fight leg during IOP20 as a function of longitude. Flight times (UTC) on 5 March 2017 are noted on each cross section. Significant terrain features of the Payette River Basin are noted. The UWKA flew flight track B during this flight.

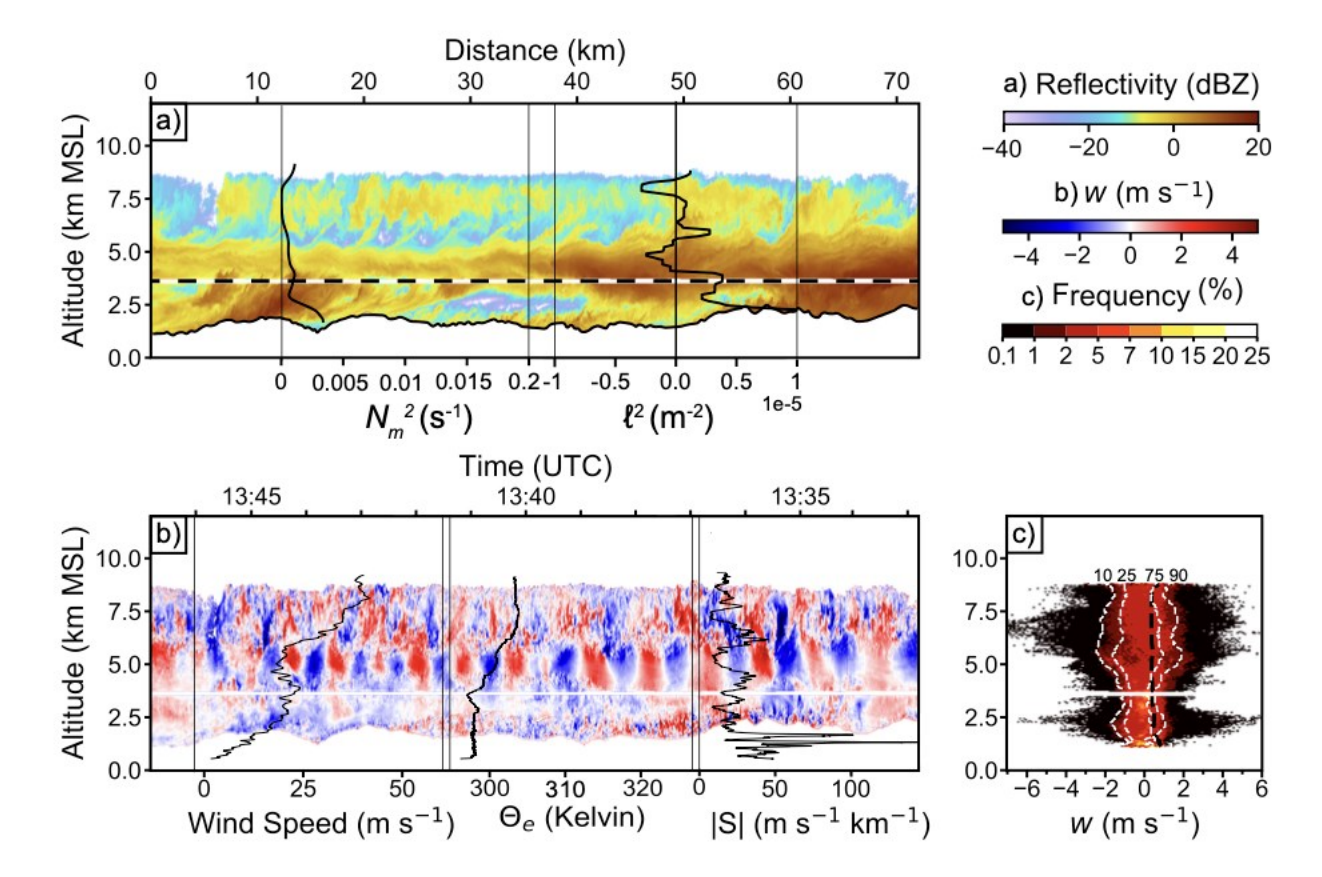


Fig. 9: WCR cross section from 5 March 2017 133250-134650 UTC. a:  $Z_e$  overlaid with  $N_m^2$  and  $\ell^2$  from a radiosonde launched at Crouch, ID at 1300 UTC; b: w overlaid with wind speed,  $\theta_e$ , and |S|: c: CFAD of w binned every 100 m in altitude every 0.1 m s<sup>-1</sup>. The black dashed line on c represents w retrieval uncertainty calculated using methodology presented in Part 1. The white dashed lines represent the  $10^{th}$ ,  $25^{th}$ ,  $75^{th}$ , and  $90^{th}$  percentiles of w at a given height. The UWKA flew flight track B during this flight.

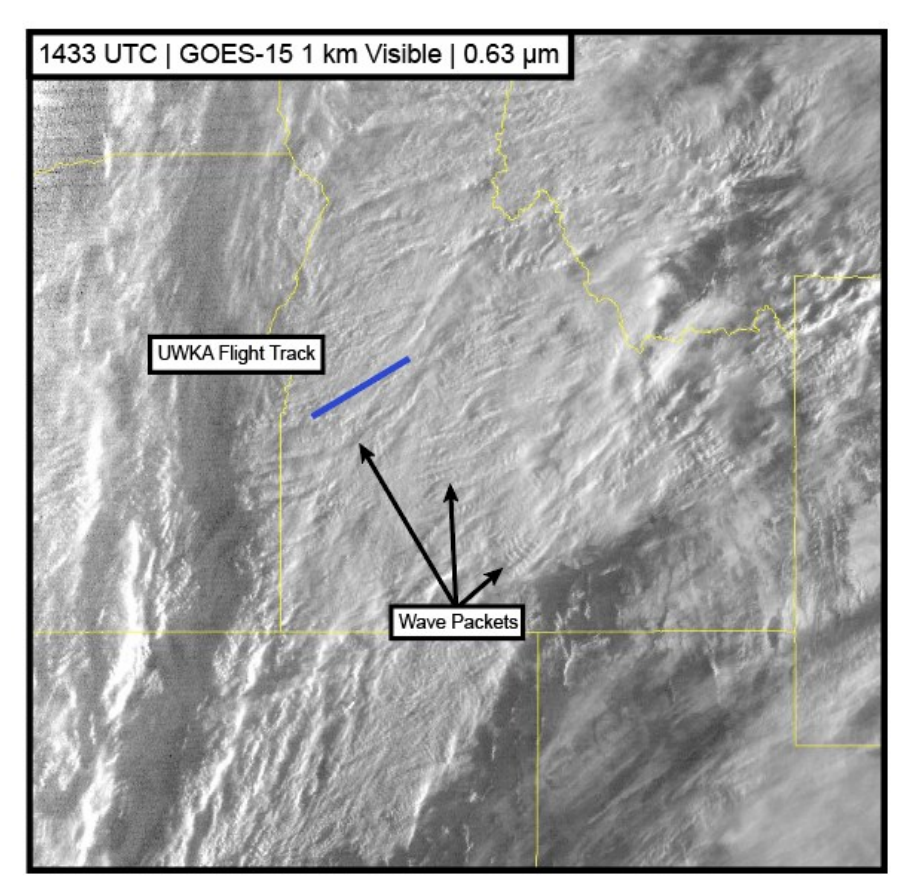


Fig. 10: GOES-15 1 km visible satellite imagery (0.63 μm) valid at 143300 on 5 March 2017. Gravity wave packets are noted. Flight track B is noted.

# b) Cloud Top Generating Cells

Generating cells are regions of locally enhanced  $Z_e$ , near cloud top from which a fall streak of hydrometeors originates (2022; AMS Glossary). Their vertical motions, microphysical properties, and forcing have been analyzed for clouds within the comma head region of extratropical cyclones (e.g. Plummer et al. 2014; 2015; Rosenow et al. 2014; Keeler 2016a,b; 2017; Kumjian et al. 2014). Cloud top generating cells have been documented on top of stratiform clouds in a variety of environments (e.g., Wang et al. 2020). They were observed at the top of orographic clouds over the Payette Basin during several SNOWIE research flights. Here we present an example from IOP1 (7 January 23 UTC to 8 January 0930 UTC) that characterizes the vertical motions within generating cells observed in other IOPs.

Fig. 11 shows generating cells present between 033130 and 035100 UTC. Clear fall streaks of locally enhanced  $Z_e$  extend downward from cloud top (Fig. 11a). In this case the fall streaks

entered a drier layer, with most losing their identifiable structure. Fig. 11c shows a CFAD typical of SNOWIE cloud top generating cells precipitating into stratiform cloud. The top km of cloud had maximum w ranging from -3 m s<sup>-1</sup> to 3 m s<sup>-1</sup>, with most measurements falling between -1.5 to 1.5 m s<sup>-1</sup>, consistent with measurements from previous studies in extratropical cyclones (e.g. Rosenow et al. 2014). Fall streaks created by the cells were only very slightly sheared, consistent with the near constant vertical profile of the wind within and just below the generating cell layer based on the IPC Crouch sounding launched at 0400 UTC (Fig. 11b). In this case, vertical wind shear had limited influence on the structure and appearance of generating cell plumes. |S| was approximately constant with height ranging from 19-28 m s<sup>-1</sup> km<sup>-1</sup> between 3 km and cloud top echo. Within the layer containing the generating cells,  $\theta_e$  remained constant with height. Keeler et al. (2016a,b, 2017) found in model simulations that generating cells are primarily driven by radiative cooling at cloud top, and can occur in the absence of environmental instability and shear. Radiative cooling at cloud top likely contributed to generating cell development during IOP1 since the flight occurred entirely at night.

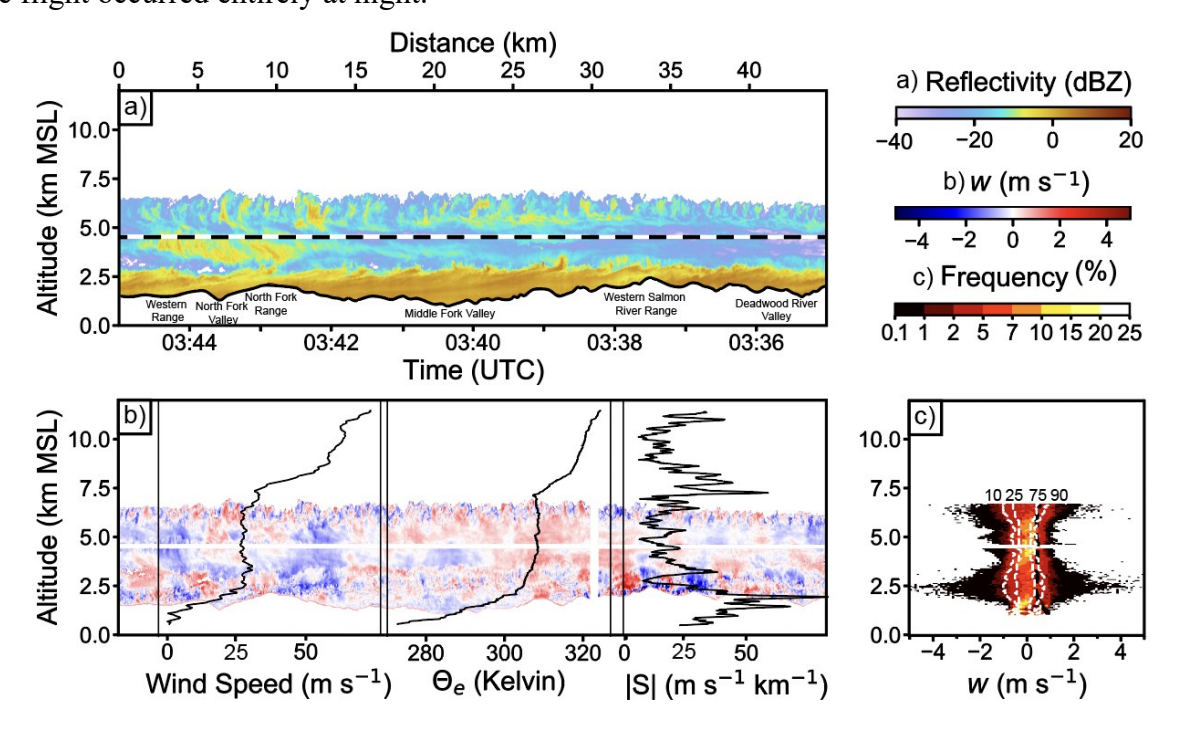


Fig. 11: WCR cross section from 8 January 2017 033130-035100 UTC. a:  $Z_e$ ; b: w overlaid with wind speed,  $\theta_e$ , and |S| from a radiosonde launched at Crouch, ID at 0400 UTC c: CFAD of w binned every 100 m in altitude every 0.1 m s<sup>-1</sup>. The black dashed line on c represents w retrieval uncertainty calculated using methodology presented in Part 1. The white dashed lines represent the  $10^{th}$ ,  $25^{th}$ ,  $75^{th}$ , and  $90^{th}$  percentiles of w at a given height. Significant terrain features of the Payette River Basin are noted. The UWKA flew flight track A during this flight.

#### c) Convection

## i) Elevated convection

During SNOWIE, there were several flights where elevated convection was observed over the Payette River Basin including IOP12 (7 February 1900 – 2330 UTC, Fig. 12a). In this case, potential instability (a decrease in  $\theta_e$  with height between 5 and 7.5 km) was present just upwind of the convection due to a dry air layer above cloud tops (Fig. 12b), based on rawinsonde data from Crouch, ID at 2000 UTC. Fig. 12b shows a strong elevated convective cell east of the Middle Fork Valley between 210430 and 210600 UTC. The CFAD in Fig. 10c shows a wide spread in w at elevations between 4.0 and 7.5 km where the elevated convection and a dry unstable layer were located. Maximum updrafts and downdrafts ranged from -6 m s<sup>-1</sup> to 6 m s<sup>-1</sup> with most vertical motions between  $\pm 2$  m s<sup>-1</sup>. Wind speed increased from 30 to 50 m s<sup>-1</sup> between 4.5 km and 6.0 km across the unstable layer, resulting in highly-sheared convection (|S| was ~25 m s<sup>-1</sup> km<sup>-1</sup> in that layer). Beneath the elevated convection between 2.0 and 4.0 km there were weak downdrafts within a strongly sheared layer where wind speed increased from 20 to 35 m s<sup>-1</sup> (|S| was ~40 m s<sup>-1</sup> km<sup>-1</sup>), leading to highly sheared fall streaks of precipitation emerging beneath the elevated convection (Fig. 12a,b).

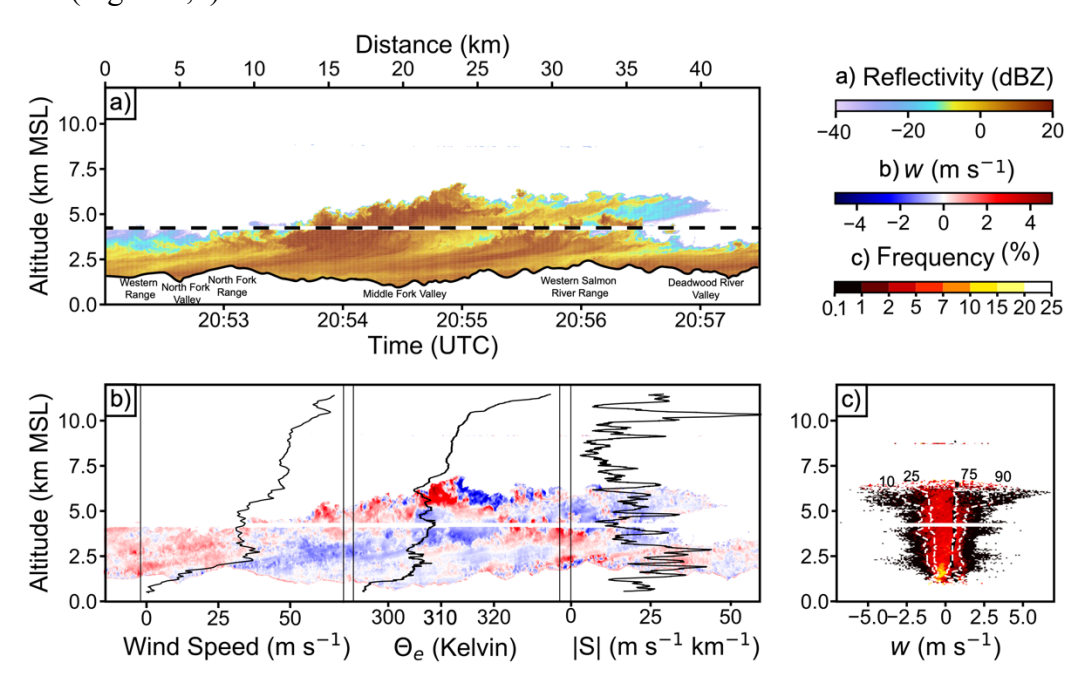


Fig. 12: Same as Fig. 11 except for elevated convection during IOP12. WCR cross section valid from 7 February 2017 205200-205730 UTC. Sounding data overlaid was collected at 2000 UTC by IPC at Crouch, ID. The UWKA flew flight track A during this flight.

# ii) Surface-based deep convection

Fig. 13 depicts surface-based deep convection extending between the boundary layer and cloud top (8 km) over the North Fork Range and Middle Fork Valley during IOP15 (19 February 1330-2330 UTC). This was the only case from SNOWIE where surface-based deep convection was observed. The convective updrafts were characterized by a broad distribution of  $w (\pm 2 \text{ m s}^{-1})$  (Fig. 13b,c). Rawinsonde data from Caldwell, ID at 1900 UTC revealed a conditionally-unstable layer between the surface and ~7 km. Wind speed increased from 4 m s<sup>-1</sup> at the surface to 20 m s<sup>-1</sup> at cloud top, resulting in a broad anvil stretching far downshear (to the right) (Fig. 13a).

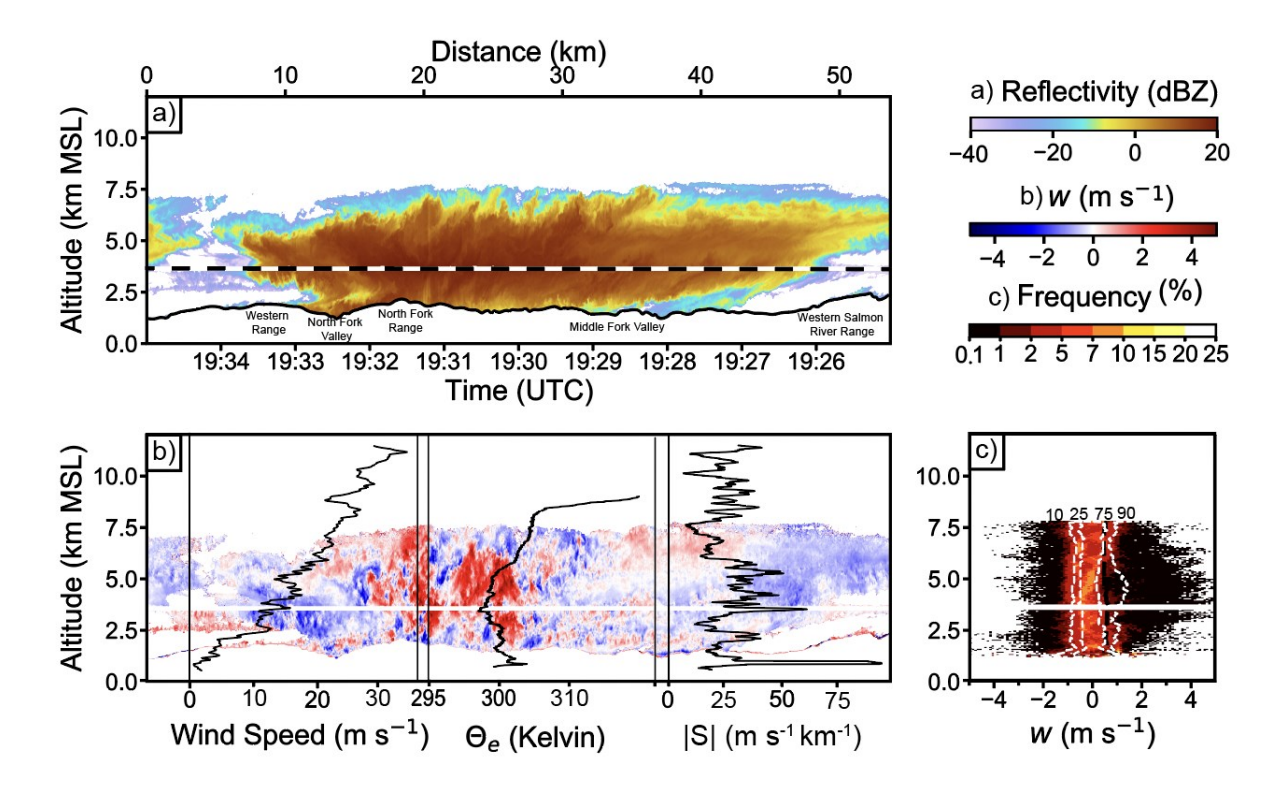


Fig. 13: Same as Fig. 11 except for surface-based convection during IOP 15. WCR cross section valid from 19 February 2017 192500 UTC to 193500 UTC. Sounding data overlaid was collected at 1900 UTC by UIUC in Boise, ID. The UWKA flew flight track B during this flight.

# d) Turbulence

# i) Boundary layer turbulence

Boundary layer turbulence was frequently observed over the mountain ranges of the Payette River Basin, especially over higher terrain. The high spatial resolution of the WCR vertical velocity field allows identification of turbulent flow by means of w power spectra (e.g., Geerts et al. 2011). IOP13 (16 February 22 UTC - 17 February 01 UTC) characterizes typical boundary

layer turbulence observed during the campaign. Fig. 14 shows an example from IOP13 between 0020-0024 UTC. Boundary layer turbulence in this case was located over the North Fork Range and Middle Fork Valley in the lowest km above the terrain with maximum values of w ranging from  $-3 \text{ m s}^{-1}$  to  $5 \text{ m s}^{-1}$ . Sounding data from Crouch, ID at 0000 UTC showed an increase in wind speed from  $5 \text{ m s}^{-1}$  to  $20 \text{ m s}^{-1}$  between 1 and 2.5 km. The  $R_i$  values within the turbulent layer were not below the critical threshold of 0.25, indicating that the turbulence was not induced by shear (Fig. 14b). Rather, the turbulence appears to be mechanically driven in the BL as air passed over complex terrain.

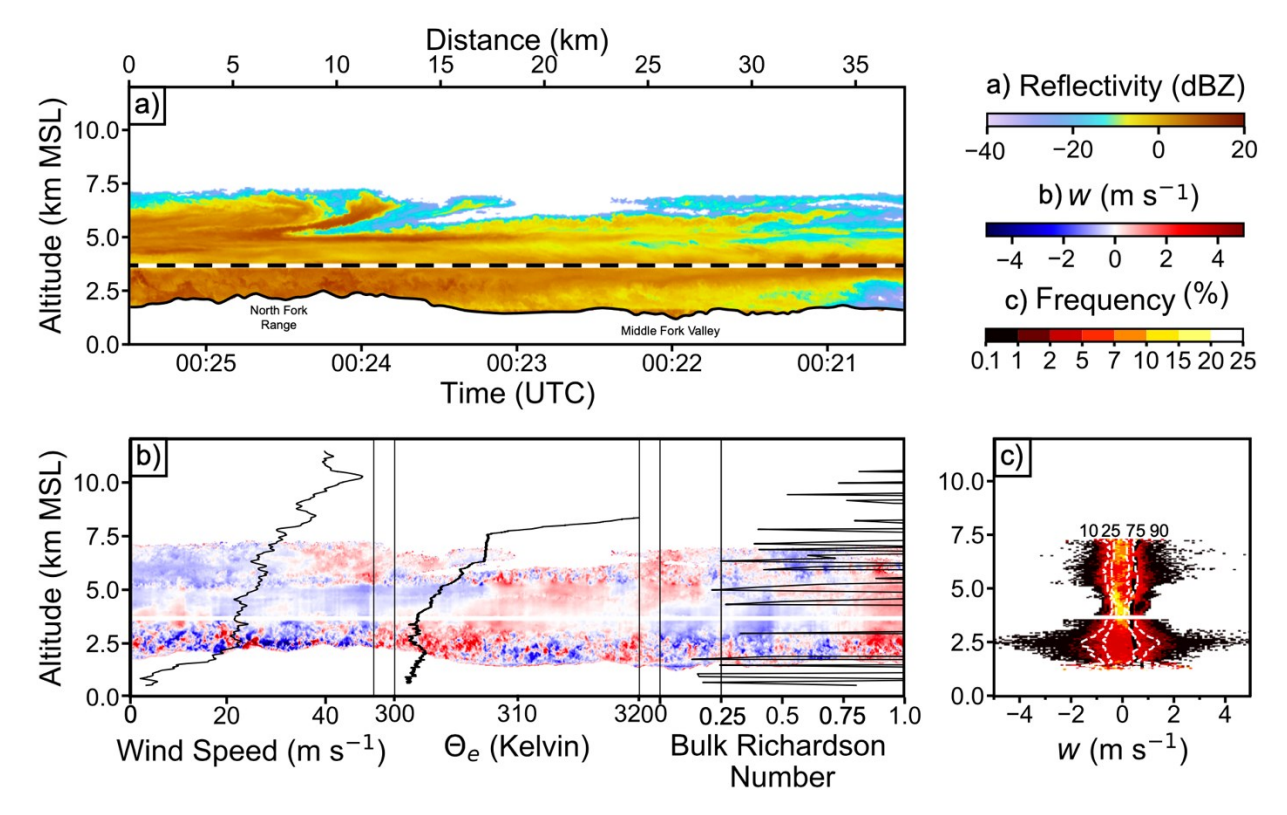


Fig. 14: Same as Fig. 11 except boundary layer turbulence during IOP 13. WCR cross section valid from 17 February 2017 002030 UTC to 002530 UTC. Sounding data overlaid was collected at 0000 UTC by IPC at Crouch, ID. Panel b is also overlaid with Bulk Richardson Number ( $R_i$ ). The UWKA flew flight track C during this flight.

## ii) Shear-induced turbulence

Shear-induced turbulence was occasionally present over the Payette River Basin. IOP16 was the most extreme example during the campaign. During IOP16 (20 February 13 – 19 UTC), a sheared layer with winds increasing from 28 m s<sup>-1</sup> to 57 m s<sup>-1</sup> was present between 5.6 and 8.0 km. The base of the shear layer was weakly conditionally unstable (Fig. 15b). A split cloud layer was

present west of the North Fork Range and over the Middle Fork Valley. The upper cloud layer was precipitating into the lower cloud layer over the Western Salmon River Range and Deadwood River Valley (Fig. 15a). Shear induced turbulence was likely in this layer as  $R_i$  was < 0.25 through much of the layer (Fig. 15b). Although most updrafts and downdrafts in this layer were  $\pm 2$  m s<sup>-1</sup>, maximum vertical motions approached  $\pm 9$  m s<sup>-1</sup> (Fig. 15c).

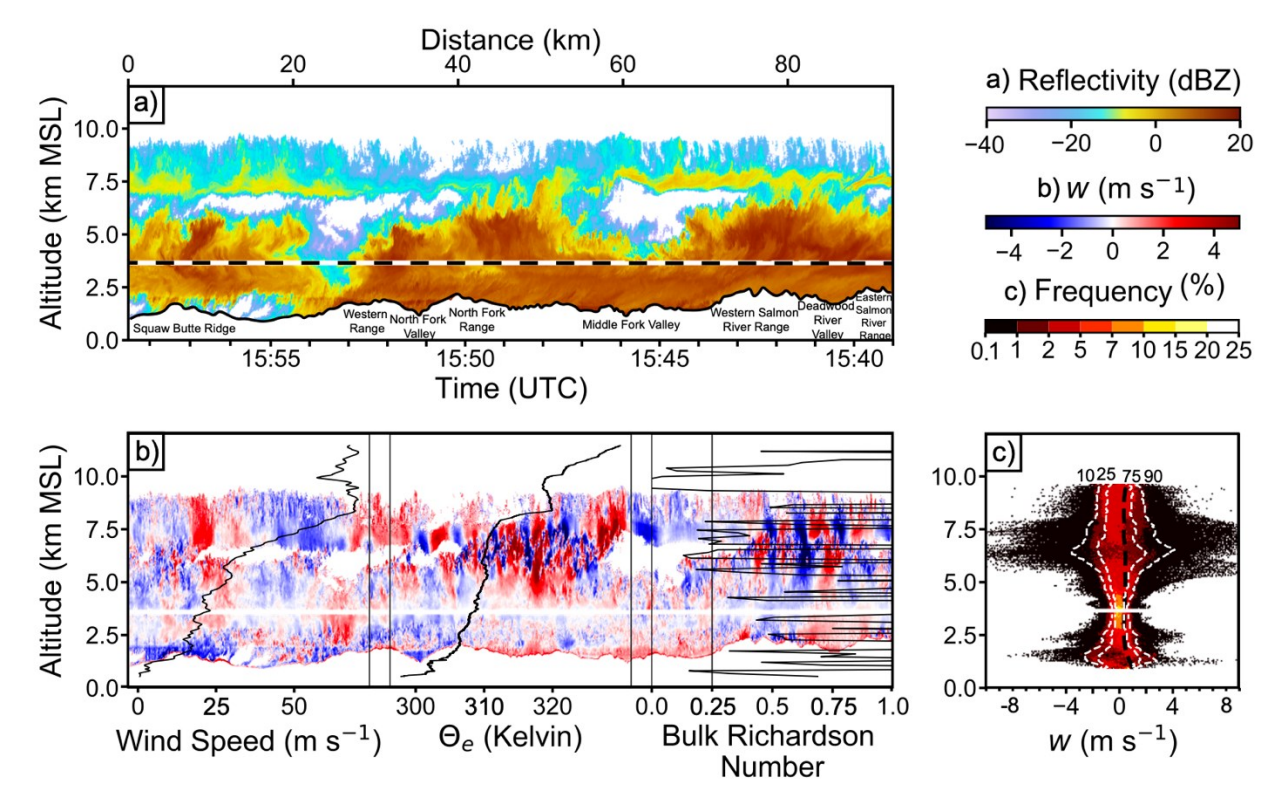


Fig. 15: Same as Fig. 11 except shear induced turbulence during IOP 16. WCR cross section valid from 20 February 2017 153900-155840 UTC. Sounding data overlaid was collected at 1500 UTC by IPC at Crouch, ID. The UWKA flew flight track B during this flight.

## **6 Discussion and Summary**

This analysis identified the sources and quantified the magnitudes of fixed and transient updrafts over the Payette River Basin of Idaho sampled during the Seeded and Natural Orographic Wintertime Clouds: the Idaho Experiment (SNOWIE). We defined fixed updrafts as those associated with stationary gravity waves in stratified flow over the orography. Transient updrafts, on the other hand, move across the terrain as a result of instability and shear associated with passing weather systems. Transient updrafts, such as surface-based convection and boundary-layer turbulence, are sometimes triggered by the underlying terrain.

Fixed vertical drafts were quantified by compositing *w* along flight tracks where the aircraft was flying parallel to mean midlevel flow. Because transient circulations vary in time and space, averaging the vertical motion fields over cross sections from a large number of flight legs effectively removed the transient updrafts while retaining fixed vertical circulations associated with the terrain. The composites revealed orographically-forced drafts with magnitudes of 0.3-0.5 m s<sup>-1</sup>. Transient updrafts are embedded in fixed vertical drafts, and typically are smaller in width and depth than the fixed drafts. Good examples are Fig. 8 in this analysis showing transient gravity waves, and Fig. 3 in Grasmick et al. (2021), showing a KH wave packet being advected through vertically propagating orographic waves.

Examples of transient vertical drafts sampled during SNOWIE were chosen from various research flights to illustrate the sources and magnitudes of updrafts and downdrafts that can occur over the terrain within winter orographic clouds. Transient vertical drafts commonly seen over the terrain during SNOWIE were associated with Kelvin-Helmholtz and other gravity waves, cloud top generating cells, elevated and surface-based deep convection, and shear-induced and boundary layer turbulence. Close-proximity soundings over the Payette River Basin were used to relate the observed vertical circulations to stability and shear profiles. Vertical circulations exceeding 2 m s<sup>-1</sup> primarily occurred in environments that were either conditionally unstable, had larger magnitudes of vertical wind shear, or both. Maximum updrafts exceeded 5 m s<sup>-1</sup> within Kelvin-Helmholtz waves, 4 m s<sup>-1</sup> associated with gravity waves, 3 m s<sup>-1</sup> in generating cells, 6 m s<sup>-1</sup> in elevated convection, 4 m s<sup>-1</sup> in surface-based deep convection, 5 m s<sup>-1</sup> in boundary layer turbulence, and 9 m s<sup>-1</sup> in shear-induced turbulence.

Cloud seeding operations in winter orographic cloud systems depend on the presence of supercooled water generated by updrafts present over complex terrain. It has, in the past, been difficult to characterize the sources and magnitudes of these updrafts because the instruments necessary to do so have not been available, or when available have not been deployed using the approach used during SNOWIE. This paper is the first to provide a thorough examination of the sources of, and magnitudes of vertical drafts that can occur when generally stratified moist flow is advected over a complex mountain range. Transient vertical circulation magnitudes sampled during SNOWIE often (but not aways) exceeded fixed vertical circulation magnitudes driven by flow over the terrain.

In Part 3 (Heimes et al. 2022), we examine whether transient vertical drafts have a significant impact on targeting during airborne cloud seeding operations, which in winter over Idaho are conducted between -12° to -15°C, temperatures which typically are found between 3 and 4 km altitude.

# 611 Appendix A: List of Variables and their Descriptions

612	dp	Change in pressure
613	g	Gravity
614	$\overset{\circ}{L}$	Latent Heat of Condensation
615	N	Brunt-Väisälä Frequency
616	$N_m$	Moist Brunt- Väisälä Frequency
617	$\Gamma_m$	Moist adiabatic lapse rate
618	$\ell^2$	Scorer parameter
619	r	Mixing ratio
620	Ri	Bulk Richardson number
621	$R_d$	dry air gas constant
622	$\theta$	Potential temperature
623	$\theta_{ m e}$	Equivalent potential temperature
624	$\theta_{ m ei}$	Equivalent Potential temperature with respect to ice
625	$\frac{\partial}{\partial v}$	Mean virtual potential temperature
626	$ heta_{v,top}$	Virtual potential temperature at top layer
627	$ heta_{v,bottom}$	Difference in virtual potential temperature between top and bottom layers
628	$ heta_v$	Virtual potential temperature
629	q	Specific humidity
630	$q_s$	Saturation mixing ratio
631	$q_w$	Total water mixing ratio
632	$q_i$	Ice mixing ratio
633	$q_l$	Liquid water mixing ratio
634	S	Vertical wind shear magnitude
635	T	Temperature
636	u	Zonal wind component
637	U	Horizontal wind component
638	$\partial U$	Change in horizontal wind
639	$\Delta u$	Change in zonal component of wind
640	$\Delta heta_{v}$	Change in virtual potential temperature
641	$V_r$	Doppler radial velocity
642	$V_t$	Terminal velocity
643	v	Meridional wind component
644	$\Delta v$	Change in meridional component of wind
645	w	Vertical velocity/updraft strength
646	$\overline{w}$	Mean vertical velocity/updraft strength
647	W	Vertical radial velocity
648	$Z_e$	Equivalent reflectivity factor
649	$\Delta z$	Change in height
650	$\partial z$	Change in height
651		

# Acknowledgments

We would like to thank the crew from the University of Wyoming King Air (UWKA) as well as all students from the Universities of Colorado, Wyoming, and Illinois for their help operating and deploying instruments during the campaign. Funding for the UWKA and WCR during SNOWIE was provided through the National Science Foundation (NSF) award AGS-1441831. This research was supported under NSF Grants AGS-1547101, AGS-1546963, AGS-1546939, AGS-2016106, AGS-2015829, and AGS-2016077. We also thank Dr. Tony Lyza, Dr. Scott Collis, and an anonymous reviewer for comments which helped substantially improve the quality of the paper.

# **Data Availability**

All data presented here are publicly available through the SNOWIE data archive website (https://data.eol.ucar.edu/master\_lists/generated/snowie/) maintained by the Earth Observing Laboratory (EOL) at the National Center for Atmospheric Research (NCAR).

- 667 References
- American Meteorological Society, cited 2013: "Generating cell." Glossary of Meteorology.
- [Available online at http://glossary.ametsoc.org/wiki/generating\_cell]
- Bolton, D., 1980: Computation of equivalent potential temperature. Mon. Wea. Rev., 108, 1046–
- 671 1053, https://doi.org/10.1175/1520-0493(1980)108,1046:TCOEPT.2.0.CO;2.
- Bruintjes, R. T., T. L. Clark, and W. D. Hall, 1994: Interactions between topographic airflow and
- cloud/precipitation development during the passage of a winter storm in Arizona. J.
- 674 Atmos. Sci., 51, 48–67, https://doi.org/10.1175/1520-0469(1994)051,0048:
- 675 IBTAAC.2.0.CO;2.
- 676 Caraceña, F., R. A. Maddox, L. R. Hoxit, and C. F. Chappell, 1979: Mesoanalysis of the Big
- Thompson storm. *Mon. Wea. Rev.*, **107**, 1–17. https://doi.org/10.1175/1520-
- 678 0493(1979)107<0001:MOTBTS>2.0.CO;2
- 679 Chater, A. M., and A. P. Sturman, 1998: Atmospheric conditions influencing the spillover
- rainfall to the lee of the Southern Alps of New Zealand. *Int. J. Climatol.*, 18, 77–92,
- doi:10.1002/(SICI)1097-0088(199801)18:1<77::AID-JOC218>3.0.CO;2-M.
- 682 Chu, C-M., and Y-L. Lin, 2000: Effects of orography on the generation and propagation of
- mesoscale convective systems in a two-dimensional conditionally unstable flow. J.
- 684 Atmos. Sci., 57, 3817–3837.https://doi.org/10.1175/1520-
- 685 0469(2001)057<3817:EOOOTG>2.0.CO;2
- 686 Chu, X., L. Xue, B. Geerts, and B. Kosovic, 2018: The impact of boundary layer turbulence on
- snow growth and precipitation: Idealized large eddy simulations. Atmos. Res., 204, 54
- 688 66, https://doi.org/10.1016/j.atmosres.2018.01.015.
- 689 Colle, B. A., 2004: Sensitivity of Orographic Precipitation to Changing Ambient Conditions and
- Terrain Geometries: An Idealized Modeling Perspective, *Journal of the Atmospheric*
- 691 Sciences, 61, 588-606. https://doi.org/10.1175/1520-
- 692 0469(2004)061<0588:SOOPTC>2.0.CO;2
- 693 Crook, N. A., 1988: Trapping of low-level internal gravity waves. J. Atmos. Sci., 45, 1533–1541.
- 694 https://doi.org/10.1175/1520-0469(1988)045<1533:TOLLIG>2.0.CO;2
- Dee, D., and Coauthors, 2011a: The ERA-Interim reanalysis: Configuration and performance of
- the data assimilation system. Quart. J. Roy. Meteor. Soc., 137, 553–
- 697 597. https://doi.org/10.1002/qj.828

- 698 Durran, D. R., 1990: Mountain waves and downslope winds. *Atmospheric Processes over*
- 699 Complex Terrain, Meteor. Monogr., No. 23, Amer. Meteor. Soc., 59–83.
- 700 https://doi.org/10.1007/978-1-935704-25-6\_4
- 701 French, J. R., K. Friedrich, S. Tessendorf, R. M. Rauber, B. Geerts, R. M. Rasmussen, L. Xue,
- M. Kunkel, and D. Blestrud, 2018: Precipitation formation from orographic cloud
- 703 seeding. *Proc. Natl. Acad. Sci.* USA, 115, 1168–1173,
- 704 https://doi.org/10.1073/pnas.1716995115.
- Friedrich, K., K. Ikeda, S. A. Tessendorf, J. R. French, R. M. Rauber, B. Geerts, L. Xue, R. M.
- Rasmussen, D. R. Blestrud, M. L. Kunkel, N. Dawson, and S. Parkinson, 2020:
- Quantifying snowfall from orographic cloud seeding. *Proc. Natl. Acad. Sci.* USA, 117,
- 708 5190-5195, doi:10.1073/pnas.1917204117
- Friedrich, K., J. R. French, S. A. Tessendorf, M. Hatt, C. Weeks, R. M. Rauber, B. Geerts, L.
- Xue, R. M. Rasmussen, D. R. Blestrud, M. L. Kunkel, N. Dawson, and S. Parkinson,
- 711 2021: Microphysical characteristics and evolution of seeded orographic clouds. *J. Appl.*
- 712 *Meteorol. Climatol.*, 60 (7), 909-934, https://doi.org/10.1175/JAMC-D-20-0206.1
- Geerts, B., Q. Miao, and Y. Yang, 2011: Boundary layer turbulence and orographic precipitation
- growth in cold clouds: Evidence from profiling airborne radar data. J. Atmos. Sci., 68,
- 715 2344–2365, https://doi.org/10.1175/JAS-D-10-05009.1.
- Geerts, B., Y. Yang, R. Rasmussen, S. Haimov, and B. Pokharel, 2015: Snow growth and
- transport patterns in orographic storms as estimated from airborne vertical-plane dual-
- 718 Doppler radar data. *Mon. Wea. Rev.*, 143, 644-665. https://doi.org/10.1175/MWR-D-14-
- 719 00199.1
- Grasmick, C., and Geerts, B. 2020: Detailed Dual-Doppler Structure of Kelvin–Helmholtz
- Waves from an Airborne Profiling Radar over Complex Terrain. Part I: Dynamic
- 722 Structure. J. Atmos. Sci. (2020) 77 (5): 1761–1782. https://doi.org/10.1175/JAS-D-19-
- 723 0108.1
- Grasmick, C., Geerts, B., Chu, X., French, J. R., Rauber, R. M. 2021: Detailed Dual Doppler
- Structure of Kelvin-Helmholtz waves from an airborne profiling radar over complex
- terrain. Part 2: Evidence for precipitation enhancement from observations and modeling.
- 727 J. Atmos. Sci. (2021), in press. https://doi.org/10.1175/JAS-D-20-0392.1

- Grasmick, C., B. Geerts, J. R. French, S. Haimov, and R. M. Rauber, 2022: Estimating
- Microphysics Properties in Ice-dominated Clouds from Airborne Ka-W band Dual
- wavelength Ratio Reflectivity Factor in Close Proximity to in situ Probes. Submitted to J.
- 731 Atmos. Oceanic. Technol.
- Heimes, K., T. J. Zaremba, R. M. Rauber, S. A. Tessendorf, L. Xue, K. Ikeda, B. Geerts, J.
- French, K. Friedrich, R. M. Rasmussen, M. Kunkel, and D. Blestrud, 2022: Vertical
- Motions in Orographic Cloud Systems over the Payette River Basin. Part 3: An
- evaluation of the impact of transient vertical motions on targeting during orographic
- cloud seeding operations. Submitted to the J. Climate Appl. Meteor.
- Hunt, J. C. R., K. J. Richards, and P. W. M. Brighton, 1988: Stably stratified shear flow over low
- 738 hills. *Quart. J. Roy. Meteor. Soc.*, **114**, 859–886, https://doi.org/10.1002/qj.49711448203
- Held, I. M, and M. Ting, 1990: Orographic versus Thermal Forcing of Stationary Waves: The
- 740 Importance of the Mean Low-Level Wind. *J. Atmos. Sci.* (1990) 47 (4), 495 500,
- 741 https://doi.org/10.1175/1520-0469(1990)047<0495:OVTFOS>2.0.CO;2
- Houze, R. A., Jr., and S. Medina, 2005: Turbulence as a mechanism for orographic precipitation
- enhancement. J. Atmos. Sci., 62, 3599–3623, https://doi.org/10.1175/JAS3555.1.
- 744 Ikeda, K., R. M. Rasmussen, W. D. Hall, and G. Thompson, 2007: Observations of freezing
- drizzle in extratropical cyclonic storms during IMPROVE-2. J. Atmos. Sci., 64, 3016–
- 746 3043, https://doi.org/10.1175/JAS3999.1.
- 747 Itoo, K., 1953: Sice, Mass and Some other Properties of Ice Crystals in the Air, 3 (4), *Japan*
- 748 *Meteorological Research Institute*, 297-306,
- 749 https://doi.org/10.2467/mripapers1950.3.4 297
- Keeler, J. M., B. F. Jewett, R. M. Rauber, G. M. McFarquhar, R. M. Rasmussen, L. Xue, C. Liu,
- and G. Thompson, 2016a: Dynamics of cloud-top generating cells in winter cyclones.
- Part I: Idealized simulations in the context of field observations. J. Atmos. Sci., 73, 1507–
- 753 1527, https://doi.org/10.1175/JAS-D- 15-0126.1.
- Keeler, J. M., B. F. Jewett, R. M. Rauber, G. M. McFarquhar, R. M. Rasmussen, L. Xue, C. Liu,
- and G. Thompson, 2016b: Dynamics of cloud-top generating cells in winter cyclones.
- 756 Part II: Radiative and instability forcing. J. Atmos. Sci., 73, 1529–1553,
- 757 https://doi.org/10.1175/JAS-D-15-0127.1.

- Keeler, J. M., B. F. Jewett, R. M. Rauber, G. M. McFarquhar, R. M. Rasmussen, L. Xue, C. Liu,
- and G. Thompson, 2017: Dynamics of cloud-top generating cells in winter cyclones. Part
- 760 III: Shear and convective organization. *J. Atmos. Sci.*, 74, 2879–2897,
- 761 https://doi.org/10.1175/JAS-D-16-0314.1.
- Kirshbaum, D. J., and D. R. Durran, 2004: Factors governing cellular convection in orographic
- 763 precipitation. J. Atmos. Sci., **61**, 682–698. https://doi.org/10.1175/1520-
- 764 0469(2004)061<0682:FGCCIO>2.0.CO;2
- Kirshbaum, D.J.; Adler, B.; Kalthoff, N.; Barthlott, C.; Serafin, S., 2018: Moist Orographic
- Convection: Physical Mechanisms and Links to Surface-Exchange Processes.
- 767 *Atmosphere*, 9, 80. https://doi.org/10.3390/atmos9030080
- Kumjian, M. R., S. A. Rutledge, R. M. Rasmussen, P. C. Kennedy, and M. Dixon, 2014: High-
- resolution polarimetric radar observations of snow-generating cells. J. Appl. Meteor.
- 770 *Climatol.*, 53, 1636–1658, https://doi.org/10.1175/JAMC-D-13-0312.1.
- Lalas, D. P., and F. Einaudi, 1974: On the correct use of the wet adiabatic lapse rate in the
- stability criteria of a saturated atmosphere. J. Appl. Meteor., 13, 318–324.
- 773 https://doi.org/10.1175/1520-0450(1974)013<0318:OTCUOT>2.0.CO;2
- Li, L., and Y. Chen, 2017: Numerical simulations of two trapped mountain lee waves
- downstream of Oahu. J. Appl. Meteor. Climatol., 56, 1305–1324,
- 776 https://doi.org/10.1175/JAMC-D15-0341.1.
- 777 Lin, Y.-L., 2009: Mesoscale Dynamics. Cambridge University Press.
- 778 https://doi.org/10.1017/CBO9780511619649
- Locatelli, J. D., and P. V. Hobbs, 1974: Fall speeds and masses of solid precipitation particles. J.
- 780 *Geophys. Res.*, **79**, 2185–2197, https://doi.org/10.1029/JC079i015p02185.
- Lyza, A. W., and K. R. Knupp, 2018: A background investigation of tornado activity across the
- southern Cumberland Plateau terrain system of northeastern Alabama. *Mon. Wea.*
- 783 *Rev.*, **146**, 4261–4278, https://doi.org/10.1175/MWR-D-18-0300.1.
- Medina, S., and R. A. Houze, 2015: Small-scale precipitation elements in midlatitude cyclones
- crossing the California Sierra Nevada. *Mon. Wea. Rev.*, 143, 2842–2870, https://doi.org/
- 786 10.1175/MWR-D-14-00124.1.
- Plummer, D. M., G. M. McFarquhar, R. M. Rauber, B. F. Jewett, and D. C. Leon, 2014:
- Structure and statistical analysis of the microphysical properties of generating cells in the

- 789 comma head region of continental winter cyclones. J. Atmos. Sci., 71, 4181–4203,
- 790 https://doi.org/10.1175/JASD-14-0100.1.
- 791 Plummer, D. M., G. M. McFarquhar, R. M. Rauber, B. F. Jewett, and D. C. Leon, 2015:
- Microphysical properties of convectively generated fall streaks within the stratiform
- comma head region of continental winter cyclones. J. Atmos. Sci., 72, 2465–2483,
- 794 https://doi.org/10.1175/JAS-D-14-0354.1.
- Ralph, F. M., P. J. Neiman, and T. L. Keller, 1999: Deep-tropospheric gravity waves created by
- 796 leeside cold fronts. J. Atmos. Sci., 56, 2986–3009. https://doi.org/10.1175/1520-
- 797 0469(1999)056<2986:DTGWCB>2.0.CO;2
- Rauber, R. M., 1987: Characteristics of cloud ice and precipitation during wintertime storms
- over the mountains of northern Colorado. J. Climate Appl. Meteor., 26, 488–
- 524.https://doi.org/10.1175/1520-0450(1987)026<0488:COCIAP>2.0.CO;2
- Reinking, R. F., J. B. Snider, and J. L. Coen, 2000: Influences of storm-embedded orographic
- gravity waves on cloud liquid water and precipitation. J. Appl. Meteor., 39, 733–759,
- 803 https://doi.org/ 10.1175/1520-0450(2000)039,0733:IOSEOG.2.0.CO;2.
- Rosenow, A., R. M. Rauber, G. M. McFarquhar, B. F. Jewett, D. Plummer, and D. Leon, 2014:
- Vertical velocity and physical structure of generating cells and elevated convection in the
- comma-head region of continental of winter cyclones. J. Atmos. Sci., 71, 1538–1558,
- 807 https://doi.org/10.1175/JAS-D- 13-0249.1.
- Shafer, J. C., W. J. Steenburgh, J. A. W. Cox, and J. P. Monteverdi, 2006: Terrain influences on
- synoptic storm structure and mesoscale precipitation distribution during IPEX IOP3.
- 810 *Mon. Wea. Rev.*, **134**, 478–497, doi:10.1175/MWR3051.1
- Sinclair, M. R., D. S. Wratt, R. D. Henderson, and W. R. Gray, 1997: Factors affecting the
- distribution and spillover of precipitation in the Southern Alps of New Zealand—A case
- 813 study. J. Appl. Meteor., 36, 428–442, doi:10.1175/1520-
- 814 0450(1997)036<0428:FATDAS>2.0.CO;2.
- 815 Smith, R. B., 2018: 100 Years of Progress on Mountain Meteorology Research. *Meteor. Monogr.*
- 59, 20.1–20.73. https://doi.org/10.1175/AMSMONOGRAPHS-D-18-0022.1
- Tessendorf, S. A., J. R. French, K. Friedrich, B. Geerts, R. M. Rauber, R. M. Rasmussen, L. Xue,
- K. Ikeda, D. R. Blestrud, M. L. Kunkel, S. Parkinson, J. R. Snider, J. Aikens, S. Faber, A.
- Majewski, C. Grasmick, P. T Bergmaier, A. Janizeski, A. Springer, C. Weeks, D. J. Serke

820	and R. Brunintjes, 2019: Transformational approach to winter orographic weather
821	modification research: The SNOWIE Project. Bull. Amer. Meteor. Soc.,
822	https://doi.org/10.1175/ BAMS-D-17-0152.1
823	Vosper, S. B., S. D. Mobbs, and B. A. Gardiner, 2002: Measurements of the near-surface flow
824	over a hill. Quart. J. Roy. Meteor. Soc., 128, 2257–2280, https://doi.org/10.1256/qj.01.11.
825	Wang, Z., J French, G. Vali; P. Wechsler, S. Haimov, A. Rodi, M. Deng, D. Leon, J. Snider, L.
826	Peng, A. L. Pazmany, 2012: Single aircraft integration of remote sensing and in situ
827	sampling for the study of cloud microphysics and dynamics. Bull. Amer. Meteor. Soc.,
828	93, 653-668. https://doi.org/10.1175/BAMS-D-11-00044.1
829	Wang, Y., G. M. McFarquhar, G. M., R. M. Rauber, C. Zhao, W. Wu, J. A. Finlon, et al., 2020:
830	Microphysical properties of generating cells over the Southern Ocean: Results from
831	SOCRATES. JGR: Atmospheres, 125, e2019JD032237.
832	https://doi.org/10.1029/2019JD032237
833	Wendisch, M. and JL. Brenquier, 2013: Airborne Measurements for Environmental Research:
834	Methods and Instruments, Wiley-VCH Verlag GmbH & Co. KGaA, Weinheim, Germany,
835	655 pp, doi: 10.1002/9783527653218.
836	Zaremba, T. J., R. M. Rauber, S. Haimov, B. Geerts, J. R. French, C. Grasmick, K. Heimes, S. A.
837	Tessendorf, Katja Friedrich, L. Xue, R. M. Rasmussen, M. L. Kunkel, and D. R.
838	Blestrud, 2022: Vertical Motions in Orographic Cloud Systems over the Payette River
839	Basin. Part 1: Recovery of Vertical Motions and their Uncertainty from Airborne Doppler
840	Radial Velocity Measurements. Submitted to J. Appl. Meteor. Climatol.